STRUCTURAL HEALTH MONITORING OF FIBER REINFORCED AND SANDWICH COMPOSITES WITH EMBEDDED FIBER BRAGG GRATING SENSORS

by

Esat Selim Kocaman

Submitted to
the Graduate School of Engineering and Natural Sciences
in partial fulfillment of
the requirements for the degree of
Master of Science

SABANCI UNIVERSITY

February 2015

STRUCTURAL HEALTH MONITORING OF FIBER REINFORCED AND SANDWICH COMPOSITES WITH EMBEDDED FIBER BRAGG GRATING SENSORS

APPROVED BY:

Assoc. Prof. Dr. Mehmet Yıldız
(Thesis Supervisor)

Assoc. Prof. Dr. Melih Papila

Assoc. Prof. Dr. Bahattin Koç

DATE OF APPROVAL: 05/01/2015

Structural Health Monitoring of Fiber Reinforced and Sandwich Composites with Embedded Fiber Bragg Grating Sensors

Esat Selim Kocaman

MAT, M.Sc. Thesis, 2015

Thesis Supervisor: Assoc. Prof. Dr. Mehmet Yıldız

Abstract

This study deals with the response of Fiber Bragg Grating (FBG) sensors embedded into fiber reinforced and sandwich composites subjected to different loading conditions and evaluates the feasibility and performance of FBG sensors for structural health monitoring. To this end, three different works were conducted. The first part investigates the effect of sensor placement into fiber reinforced composites on the acquired signal quality during the fatigue loading. In the second part, the performance and behavior of FBG sensors embedded inside fiber reinforced composites are studied under constant, high strain fatigue loading conditions in order to assess the mechanical energy, strain distribution and evolution along the specimen. In the context of the second section, the evolution of temperature in composites specimen due to autogenous heating is monitored employing a set of thermocouples. In the final part, three different failure modes of foam cored sandwich composites, namely, facing indentation, compressive facing and core shear failure are monitored by using spectrum and wavelength information of embedded FBG sensors.

Fiber Takviyeli ve Sandviç Kompozitlerin Gömülü Fiber Bragg Izgara Sensörler ile Yapısal Sağlık İzlemesi

Esat Selim Kocaman

MAT, M.Sc. Tezi, 2015

Tez Danışmanı: Doç. Dr. Mehmet Yıldız

Anahtar Kelimeler: *Fiber takviyeli polimer kompozitleri, sandviç kompozitler, yorulma, fiber Bragg ızgara sensörler (FBG), yapısal sağlık izlemesi*

Özet

Bu çalışma farklı yükleme koşulları altındaki fiber takviyeli ve sandviç kompozitlerin, gömülü fiber Bragg ızgara (FBG) sensörleri kullanılarak yapısal sağlık izlemesini incelemektedir. Bu bağlamda üç farklı çalışma yürütülmüştür. İlk kısımda fiber takviyeli kompozitlere sensor yerleştiriminin yorulma yükü sırasındaki sinyal alım kalitesine olan etkisi incelenmektedir. İkinci kısımda numune üzerindeki mekanik enerji, gerinim dağılımı ve gelişimini değerlendirmek için fiber takviyeli kompozitlere gömülmüş FBG sensörlerin yüksek gerinimli, sabit yorulma yükleri altındaki performans ve davranışları araştırılmıştır. Bu bağlamda, termokupl kullanılarak numune üzerinde yorulmaya bağlı olarak oluşan sıcaklık değişimi görüntülenmiştir. Son kısımda ise, köpük çekirdekli sandviç kompozitlerin 3 farklı hasar modu; yüz indentasyonu, yüzde oluşan basma kırılması ve çekirdek kayma hasarı, gömülü FBG sensörlerden alınan spektrum ve dalgaboyu bilgisi kullanılarak izlenmiştir.

To my family…

ACKNOWLEDGEMENT

Table of Contents

List of Figures

List of Tables

CHAPTER   1

Introduction

1.1. Motivation and Literature Review

1.1.1. Fiber Reinforced Composites

Composite materials are composed of more than one phase that is artificially mixed together. They contain fibrous or particulate fillers embedded in a certain matrix. Matrix material can be polymer, carbon, metal, ceramic or their combination [1]. Combination of more than one different material heterogeneously enables one to obtain composite material with outstanding properties that cannot be achieved using each ingredient separately. In the scope of this thesis work, focus was on the polymer-matrix composites specifically one composed of thermoset polymer matrix and continuous fiber filler.

Composite materials with their high specific strength and stiffness provide excellent opportunities for weight reduction in structural components used in a variety of industries ranging from automotive, civil infrastructure to aerospace. Reducing the weight in transportation industries through use of composites provides great potential in fuel savings making them very crucial structural materials. Increased application of composites necessitates understanding of the material behavior in variety of loading and environmental conditions. In almost all of the applications, composite components are exposed to cyclic loadings. Thus, investigation of the fatigue in composites is very crucial in terms of their reliable real-life implementation. One of the drawbacks of these materials is their heterogeneous nature making their behavior highly complex to predict. This resulted in great amount of work in literature and there are still many issues in composite that requires careful examination to reveal response of composite structures under different loading conditions.

Unlike metals, composite materials show various damage mechanisms when exposed to cyclic loads. Damage accumulation takes place in a general rather than localized fashion, and failure does not necessarily occur by the propagation of a single macroscopic crack as in the

case of metals. These micro-structural damage mechanisms of the composites include matrix cracking, debonding, delamination, transverse-ply cracking and fiber breakage. Such damage mechanisms can take place independently and interactively, and testing conditions and material types can significantly affect the predominance of any damage accumulation mechanism over the other. At early stages of the fatigue loading, damage is distributed and occurs progressively causing potential reductions of both strength and stiffness of the loaded section [2].

The effect of fatigue loading causes stiffness of fiber reinforced polymer matrix composites to follow a certain trend encompassing different stages. In Figure 1.1, there is an illustration of the resulted stages of stiffness degradation. At Stage I, a rapid and convex decrease in stiffness is observed which can be attributed to a rapid interconnection of matrix cracking initiated by shrinkage stresses, degree of resin cure, voids and fiber discontinuities. This stage generally encompasses the first 15-25 % of fatigue life. Stage II is described by a gradual, linear decrease in stiffness that occurs between 15-20 % to 90-95 % of the fatigue life. This decrease is attributed to matrix cracking leading to crack propagation, fiber debonding and delamination. At the final stage fiber breakage occurs which accounts for the rapid, nonlinear decrease eventually resulting in a sudden specimen failure [3].
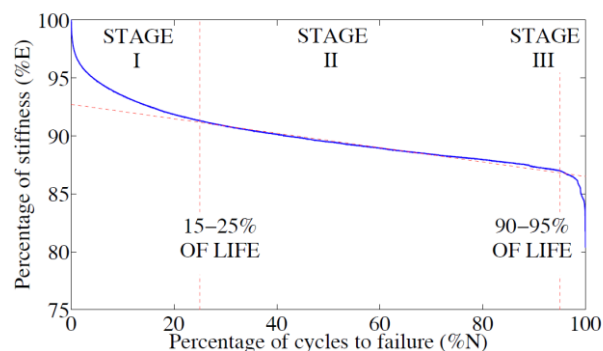
Figure 1.1: Stiffness degradation vs. fatigue cycle.

Currently, composite structures are built with high safety factors in order to compensate for the variability in manufacturing and lack of accurate prediction methods among other factors. Such practices result in overweight structures that require periodic maintenance to detect damage. In order to fully exploit the performance of fiber reinforced composites, their structural health monitoring is very essential which can allow failure and damage detection of structural components under real-time operating conditions. Successful implementation of such a system within composite structures can decrease the maintenance costs significantly and increase the inspection intervals leading to great economic savings. One methodology to

perform structural health monitoring is embedding fiber optic sensors known as fiber Bragg gratings (FBG) within the composite material during manufacture and monitoring the sensor response as loads induced in the structure. This system can provide real time knowledge of the "health" of the structure during operation allowing the composite structures to be built with a lower safety factor and operated for longer life cycles.

1.1.2. Fiber Bragg Grating Sensors

Fiber Bragg Gratings (FBG) optical sensors are gaining increased importance thanks to the several attributes it possesses enabling it to be utilized for a variety of applications. These features include but not limited to immunity to electromagnetic interference, multiplexing potential, high signal resolution capacity and suitability for embedment into structural components [1]. Basically, a FBG sensor is a short section of an optical fiber with a periodic variation in the refractive index of the fiber core generating a wavelength specific dielectric mirror. Thus, it acts as an optical filter by allowing a broad band of light to pass while reflecting a narrow band centered on a wavelength known as the Bragg wavelength λ_B. The reflected wavelength is a function of the grating pitch, Λ (i.e., spacing between the refractive index variations) and the average refractive index, η and satisfies the Bragg condition as $\lambda_B=2\eta\Lambda$. Spacing between the refractive index variations is sensitive to the variations of both strain and temperature which in turn shifts the Bragg wavelength leading to the following condition,

$$\frac{\Delta\lambda}{\lambda_B} = (1 - p_e)\varepsilon + (\alpha + \xi)\Delta T \tag{1}$$

Where $\Delta\lambda$ is change in the wavelength, p_e is the photo-elastic coefficient, α and ξ are thermal expansion and thermo-optic coefficient of fibers, respectively. ε is the strain and ΔT represents the temperature change of the sensor [4]. These sensors can offer very good linear correlation between strain and the wavelength response.

Photosensitivity is the phenomenon that is exploited to produce the FBG sensors and it refers to the permanent change of refractive index of the material by exposure to light. There are three main approaches to fabricate FBG sensors which include interference, phase mask and direct-write. Grating length, complexity of design and strength are the crucial factors to consider in order for choosing appropriate fabrication methods [5]. For the interference technique, a laser beam is first split and recombined at an angle and in the fiber segment

where the beams overlap, interference patterns occurs. To introduce the desired grating periodicity recombination angle and laser wavelength have to be tuned. For phase mask technique, fiber is placed in close contact with the mask having periodic patterns usually etched onto fused silica. When the laser beam is sent through the mask, it creates diffractive order and interference gives rise to desired intensity patterns recorded into the fiber. Period of the grating is the half of the phase mask periodicity for normal incidence of the laser light. This technique is suitable for high volume production and hence more ideal for commercialization. In the last approach, by moving fiber and phase mask which is exposed to normal laser beams with respect to each other, small number of fringes are formed and stitched together. The width of the laser beam determines the wavelength shift and this system is capable of providing desired phase shifts and apodization for the FBG sensor [5].

Generally, the sensitivity of strain and temperature of a bare FBG is around 1.2 *pm/με* and 13.7 *pm/^oC*, respectively, however it is crucial to measure the strain and temperature sensitivity of every embedded FBG sensors as factors such as variation in material properties and manufacturing tolerance might alter the sensitivity and to account for the strain transfer between the sensor and the host material [6].

Dependency on strain and temperature can be utilized to design sensors to measure properties such as displacement, strain, temperature, pressure, humidity, and radiation among others. There are significant efforts in the literature to design chemical sensors [5], humidity sensors [7][8], biosensors [9] and strain sensors [10][11] in this context. Another crucial application of FBG sensors is the structural health monitoring of civil and geologic structures [12]. Using a variety of sensor designs, strain data of various structures in civil infrastructure can be detected reliably for real-time condition monitoring. This application of FBG sensors is at the commercialization phase and real-life condition monitoring FBG based sensor systems are becoming increasingly widespread especially for bridges [13][14][15].

Another crucial feature of FBG sensors is that they are light weight, flexible and very thin allowing them to be compatibly embedded in fiber reinforced composite structures without significantly affecting the structural integrity making them very promising sensors for condition monitoring of composite structures. There are significant amount of work dealing with SHM of composite structures using FBG sensors which also forms the center of this thesis and brief review of the literature is provided in the following.

Detection of damage and monitoring internal strains of composite structures using embedded fiber optic sensors has been extensively studied by various researchers. In many of these works, the focus was on the investigation of FBG response to transverse cracks and

delaminations formed in the proximity of sensors due to either static and fatigue loading conditions. These researchers attempted to characterize the change in the reflected spectrum of a long gage FBG to detect and measure the crack density [16], [17], crack locations [18] and delamination length [19], [20]. Takeda et al presented a novel methodology to observe and model the microstructure damage evolution in quasi-isotropic composite laminates by using optical microscope and a soft X-ray radiography and damage mechanics analysis. They also introduced another methodology where they monitored the transverse crack evolution by correlating it to optical power loss [21]. Yashiro et al, proposed a numerical approach to link the reflection spectrum distortions of the embedded FBG sensor to multiple damage states of the laminate. When compared to the results of quasi-static testing of the notched CFRP cross-ply laminates, rather good correlations were achieved [22]. Takeda et al introduces new technique to estimate the damage patterns of notched composite laminates with embedded FBG sensors. By utilizing a layer-wise finite element model that represents the transverse cracks as cohesive elements, damage pattern and applied strain were derived from the reflected spectrum as an inverse problem and it was shown that they agree with the experimental data [23]. Doyle et al. performed in-situ process and condition monitoring to evaluate different fiber optic sensor systems and acquired a rather good correlation for the strains between the surface mounted strain gages and optical sensors. They demonstrated the feasibility of the sensors systems to monitor the stiffness degradation due to fatigue [24]. Baere et al. evaluated the performance of embedded and bonded Bragg grating sensors specially coated with Organic Modified Ceramic to measure strains in carbon fiber reinforced thermoplastic composites under fatigue loading conditions. They successfully demonstrated the durability of the FBG sensors over half a million loading cycles and compared the FBG and extensometer measurements for the strain by applying static tests after every 40200 cycle of the fatigue loading. Upon comparison of the static test results, it was revealed that two strains quantities agree well with each other demonstrating the feasibility of the sensing system [25].

Moreover, FBG sensors were employed for ultrasound detection within structures where piezoelectric transducers send surface waves through the material while FBG sensors are used to detect the waves [26], [27]. Their SHM capability was also studied for damage detection of impact damaged cross-ply CFRP laminates [27]. In other works, effect of non-uniform strains onto the response of FBG sensors with different lengths (i.e., 5 mm-10 mm long) embedded in a neat epoxy specimen were inspected to correlate the strain distribution with the spectrum response [28][29]. These works have demonstrated that as long gage length

FBGs are vulnerable to uneven strain fields, they can experience peak distortions and splitting in the reflected spectrum.
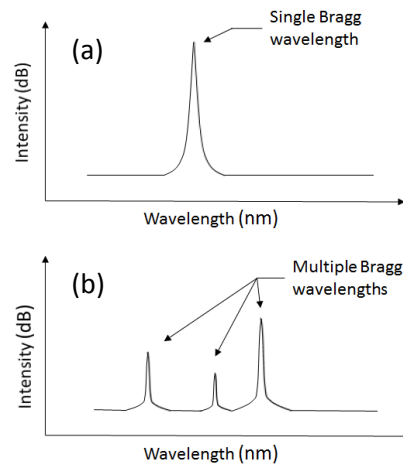
Figure 1.2: Schematics for reflected FBG spectrum from even strain field **(a)** and peak splitting resulting from uneven strain field **(b)**

Figure 1.2a shows a typical signal from an embedded FBG under an even strain field. As observed, a narrow, clean, symmetric peak is reflected back from an FBG. When the FBG is exposed to an uneven strain field, different segments of the FBG are under different magnitudes of strain and therefore reflect a wavelength corresponding to the strain of that length as FBG acts as a number of smaller FBGs. This can cause reflection of more than one Bragg wavelength which is known as peak splitting as it is shown in Figure 1.2b. When embedded within a composite, a typical FBG with 10mm length is exposed to a variation of strain magnitude due to the composition of the composite (stiff fibers and a compliant matrix). This results in the aforementioned situation of an uneven strain field, which causes the peak to split whereby a typical interrogation system can no longer detect the peak signal. The use of a shorter FBG, 1mm in length that is aligned with the reinforcement fibers in the composite has the potential to experience a less uneven strain field and therefore produce an acceptable signal possessing more reliable physical information.

Furthermore, there are significant works dealing with the effect of thermal residual stresses on the reflected spectrum of FBG sensors. In the work of Okabe et. al., it was found that effect of thermal residual stresses onto the reflected spectrum distortions can be decreased when the optical fiber was coated with polyimide [30]. FBG sensors are also utilized for remaining useful life analysis for composites under fatigue loadings [31]. Another important area where FBG sensors are extensively studied is the cure monitoring of composite structures [32][33][34].

1.1.3. Sandwich Composites

Sandwich composites are fabricated by connecting two stiff laminated composite facings with lightweight thick core. This structure provides high specific flexural stiffness leading to considerable weight savings [35]. And such attractive features make sandwich composites ideal material choice in a variety of industries ranging from naval, aerospace to civil infrastructure. Facings of the sandwich structure are designed to bear compressive and tension loads while the core is mainly responsible for carrying the shear loads similar to I beam mechanism [36]. As the material posses highly heterogeneous structure, it shows highly complex behavior to different loading and environmental conditions and various damage mechanisms can form in response during their service life [37]. In this study, investigation focus was on the foam-cored sandwich composites especially ones consists of PVC structural foam cores. Prominent failure modes that such structure faces during their lifetime are facing indentation, core crushing, facing failure due to compression and core shear failure [38-41]. There are crucial properties which highly affect the overall structural performance of sandwich composites. Bonding between the core and facings is one of the crucial factors as it determines the adequate stress transfer through the interface [42]. The defects emerged in the manufacturing process or cyclic and impact service loading conditions can cause inadequate bonding between the facing and the core resulting in failures between core and the facing. Compressive strength and density of the core has also great significance as it highly effects the formation of core crushing and facing indentation as the prominent damage modes. Moreover, impact loads can cause local indentation failures endangering the structural integrity [43]. Thus, it is highly relevant to detect the damage formation in order to assess the structural reliability of the components during their service life. Inherent failures caused by the core shear failure and indentation necessitate the periodic non-destructive examination/testing of the structure as visual detection is not plausible. This inspection procedure is costly process and as the structure taken out of service, this further increases the lost revenue. In order to circumvent this problem, a sensor system can be installed to the desired parts in order to monitor the real time structural integrity or "health" of the component. One of the most promising methods for structural health monitoring currently under study is based on Fiber Bragg grating (FBG) sensors embedded within the composite facings during manufacturing.

In the literature, there is restricted number of works dealing with the monitoring of sandwich composites behavior under different loading conditions using FBG sensors. One of

the prominent works in this area is done by Kuang et al. where they used FBG sensors in order to monitor the manufacturing process of sandwich composites made of aluminum foam core and hybrid facing with glass fiber reinforced thermoplastic and aluminum layers [44]. Furthermore, the wavelength shift of the FBG sensor is utilized to detect the melting and solidification of the system in question. Moreover, they performed cyclic three-point bending tests on the sandwich composites in order to evaluate the structural integrity through using FBG sensors [45] and determining corresponding damage parameter as introduced in the literature [46]. Another prominent work is conducted by Hackney et al. where repetitive low velocity impact loads were applied to foam cored sandwich plates with embedded FBG sensors to monitor the residual strains and spectrum changes during the test in order for correlating sensor responses to different damage modes occurred in the specimens [43].

1.2. Outline of the Thesis

Scope of this thesis is the investigation of fiber reinforced and sandwich composites under different loading conditions using embedded FBG sensors and evaluate the feasibility and performance of these optical sensors to achieve structural health monitoring. To this end, three different works were conducted and this thesis is the compilation of these works.

First part studies the effect of sensor placement into fiber reinforced composites on the signal acquisition quality during the fatigue loading. Obtaining a clear signal is highly important in terms of reliability of the measured strains. As explained in the previous sections, when FBG sensor experiences a non-uniform strain field along its gagelength, this can result in splitting of the reflected spectrum acquired from the sensor. In order to evade this problem, this work proposes certain practical factors that require consideration in order to obtain continuous data acquisition. These factors include proper selection of FBG length and orientation with respect to adjacent fibers, tow width with respect to FBG length and crack density. When 10mm FBG sensors embedded perpendicular to the reinforced fibers and exposed to fatigue loading, intermittent loss of signal occurs which might be attributed to the formation of damage in the composite that create dynamically varying strain field in the proximity of the FBG sensor. Such behavior is not observed for 1mm FBG sensors indicating the importance of the proposed practical factors.

For the second part, response of FBG sensors embedded inside glass reinforced composites are monitored under low-cycle fatigue loading conditions in order to assess the mechanical energy, strain distribution and evolution along the specimens. Understanding FBG

response under low-cycle fatigue conditions is important in terms of applicability of these sensors to monitor structures that are exposed to repetitive high dynamic loads. Furthermore, this works also proposes important considerations for the implementation of strain-controlled fatigue tests using two different methods based on extensometer and LVDT which is also crucial for proper characterization and understanding of the material behavior. Three consecutive FBG sensors written along the same fiber optic cable were integrated along the specimen gagelength in order to study the strain distribution during the uniaxial fatigue loading. In this work, it is shown that strains from the sensors located in different locations can decrease as the test progress which can be attributed to the relaxation related to the damage in the vicinity of the FBG sensors. Furthermore, measured sensor strains can significantly deviate from each other as low-cycle fatigue progress. This notifies the distinction between the global and local strains of the loaded specimen suggesting the importance of the consideration of the local behavior when analyzing composite structures under such conditions.

In the last part, failure modes of foam core sandwich composites are investigated by monitoring three different failure modes i.e. facing indentation, compressive facing and core shear failure using embedded Fiber Bragg Grating (FBG) sensors. The understanding of the strain evolution induced by flexural loading and the FBG response to different damage states in sandwich composites is crucial in terms of applicability of these sensors into real structures. Exploiting how sensors respond to a particular damage mode by tracking the wavelength shift and spectrum information, failure detection strategy is developed for damage characterization to perform condition monitoring of sandwich structures.

CHAPTER   2

An Experimental Study on the Effect of Length and Orientation of Embedded FBG Sensors on the Signal Properties under Fatigue Loading

2.1. Introduction

Fiber Bragg Grating sensors provide excellent capability for structural health monitoring (SHM) of load bearing structures through allowing for local internal strain measurements within structures. However, the integration of these sensors to composite materials is associated with several challenges that have to be addressed in order to have correct strain measurement and in turn perform reliable SHM. One of the most important challenges with embedded FBGs in composite materials operated under fatigue lies in obtaining a clear and accurate signal. Matrix cracking and the orientation of adjacent reinforcement fibers may cause uneven strain fields in the grating resulting in peak splitting, which causes an offset in the reading obtained from the sensor. With proper FBG selection and reinforcement fiber orientation, these problems might be reduced or even eliminated. In this work, it is demonstrated that long FBG sensors (i.e. 10 mm) embedded inside fiber reinforced composite specimens being subjected to uniaxial fatigue loading in the sensor direction can show distortion and splitting in the reflected spectrum and can even experience intermittent loss of the signal even though they are not initially and particularly positioned nearby the non-homogeneous strain field. This intermittent loss of signal might be attributed to the formation of damage in the composite that create dynamically varying strain field in the proximity of the FBG sensor. It is further shown that short gage length FBGs (i.e. 1 mm) are much more immune to such strain fields and their spectrum is less likely to be distorted by the uneven strain distribution, hence leading to much more reliable strain measurement than the long FBG sensors as their spectrum is largely intact. Moreover, this work investigates the reasons causing peak splitting of FBG sensors once embedded into composite structures subjected to fatigue loading and proposes a few important and practical factors (i.e., the tow width should be greater than the length of the FBG, the optical fiber should be aligned with the direction of the adjacent reinforcement fibers, ideally the crack density should be equal to

or greater than the FBG length) that needs to be taken into account to circumvent its occurrence.

2.2. Experimental Investigations

To investigate the potential benefits of a shorter FBG and factors affecting the quality of acquired signals from longer FBG, a number of experiments have been performed. Both 10mm and 1mm long FBGs have been embedded in a glass fiber/epoxy composite and subjected to fatigue loading until failure. During loading the signal from the FBG is monitored. After failure the specimens are sectioned to acquire the relevant cross-sections which were polished and examined under optical microscope.

2.2.1. Materials and Sensors

The laminate selected for this research is $[(0/90)_6]_S$ and $[(90/0)_6]_S$, glass fiber with epoxy resin. The fiber used is Metyx LT300 E10A 0/90 biaxial E-glass stitched fabric with 161gsm in the 0° orientation and 142gsm in the 90° orientation, summing to 313gsm total. The selected resin is Araldite LY 564 epoxy resin with XB 3403 hardener produced by Huntsman Corporation. The panels undergo an initial cure at 65 ^{o}C for 24 hours with a post cure at 80 ^{o}C for 24 hours. Figure 2.1 shows a sample of the fabric with a ruler overlaid for reference. The tow width is measured to be roughly 2mm. The FBG sensors used in this work are from FiberLogix. They have a center wavelength of 1555nm or 1540nm and lengths of either 10mm or 1mm.
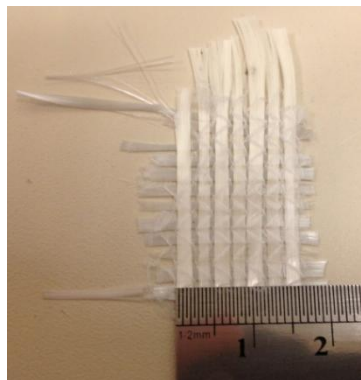
Figure 2.1: Fabric tow width (~2mm).

2.2.2. Fatigue Specimen Preparation

A number of processing methods exist for composite materials. One method that is particularly suitable to produce composite parts satisfying stringent specifications of the aircraft industry is the Resin Transfer Molding (RTM) technique. RTM can produce high quality near net-shape parts with high fiber volume fractions, two high quality surfaces and little post processing in a fully contained system that eliminates human operator exposure to chemicals and reduces the chance of human error. For these reasons, RTM has been selected to produce the specimens for this study. A sophisticated laboratory-scale apparatus was designed and built with the ability of embedding fiber optics into the composite component. This apparatus is used to produce flat panels that are 620mm x 320mm x 3.5mm, which are processed into specimens for fatigue testing. All specimens have fiber optics embedded in the mid-plane of the laminate. Depending on the configuration of the laminate $[(0/90)_6]_S$ or $[(90/0)_6]_S$, the FBG is perpendicular to or in line with the glass fibers, respectively. This proves to be an important detail in terms of data collection as discussed later. A tabbing material composed of 1.5mm thick, plain weave E-glass fabric/epoxy with a ~20° angle on one edge is bonded with West System 105 epoxy and 205 hardener thickened with milled glass fiber with a bond-line thickness of 0.7mm. The panels are cut into specimens using a water-cooled diamond blade saw and the edges of specimens are polished by sandpapers with up to 400 grit. The final dimensions of the fatigue specimens are 280mm x 15mm x 3.5mm with a 160mm gage length. The length of the specimen is aligned with the 0° fiber orientation. Figure 2.3a shows a drawing of the specimens. A special fixture is required to grip the specimen such that the fiber optic ingress location is not under load. The fixture consists of three steel plates, a bar and a pin. Two plates are clamped across either side of the specimen with bolts. One plate has a slot that allows the fiber to egress from the composite. The plates are screwed into the third plate that has a cylindrical pin that interfaces with the machine grips. A stiffening bar is located across the slot to reduce detection when the bolts are tightened. Figure 2.2b shows this fixture.
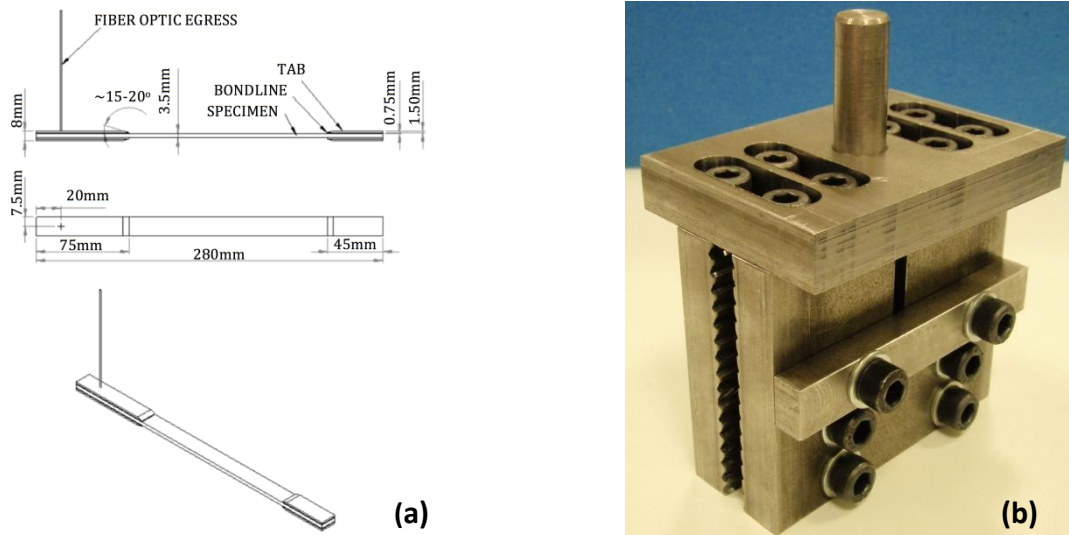
Figure 2.2: a) Drawing of test specimens, and **b)** gripping fixture.

2.2.3. Fatigue Loading

Many challenges lie in the area of fatigue testing of composite materials. They exhibit different characteristics from metallic materials that become apparent during fatigue testing. One such difference between metallic and composite materials is their heat conduction. Autogeneous heating becomes a major concern during fatigue testing of glass fiber reinforced composites as the built up heat is not conducted to the environment as it is with metallic materials. The fatigue properties of composite materials are especially sensitive to heat. ASTM standard D3479 states that a temperature increase of 10°C has demonstrated measurable property degradation. Generally a fatigue loading frequency of 1-4 Hz for glass fiber has been used with no or negligible heating [47]. This results in a lower testing frequency, which in turn results in extended time to perform an adequate test study. All fatigue tests were conducted with tension-tension sinusoidal load at 4Hz. Fatigue loading was applied under displacement controlled mode with maximum displacement corresponding to a constant amplitude strain of 0.4 and 0.5 times the ultimate strain of the material. The maximum and minimum loads and displacement are recorded from the MTS software. The minimum stress on the specimens is 27.6MPa while the maximum load is determined as a fraction of the maximum stress of 318.75MPa; 0.4 or 0.5 depending on the test. The magnitude of the minimum load was selected based on the value used by Natarajan et al. [15] in a similar fatigue study to prevent the generation of compressive loads. To determine the displacement amplitude to obtain the desired strain, a simple calibration procedure is

performed: the specimen is loaded into the machine and a load that will produce the desired amount of stress is slowly applied and released, then applied and released a second time. When the specimen is unloaded there is a residual displacement sensed by the LVDT. This is due to the wedge grips tightening and the specimen slipping slightly before the full clamping force is realized. To account for this nonlinear phenomenon the zero-offset/residual displacement value is subtracted from the maximum displacement on the second loading cycle. The peak of the FBG was interrogated with a Micron Optics SM230 interrogator at a rate of 100Hz.

2.2.4. Microscopic Inspection

To prepare samples for the microscopic inspection, sections were cut from the full size specimen after having been subjected to fatigue testing. Initially, three small samples were cut perpendicular to the loading direction from the center of each fatigue test specimens using a water cooled circular diamond saw. In order to investigate the cracks located along the fiber direction, samples are also cut parallel to the loading direction such that the optical fiber is as close as possible to the cut surface. All cut surfaces were polished on a rotating lap by progressive abrasion using finer and finer grits of silicon carbide sand paper and then investigated under an optical microscope with dark and bright field reflected light mode.

2.3. Results and Discussion

FBG data were recorded during testing and the specimens were inspected under a microscope after failure to determine the crack density. The effects of the different FBG lengths and orientations are quite evident in the collected data. Essentially, with a 1mm long FBG that is oriented in-line with adjacent reinforcement fibers, there is no lost data (data recorded as 0 due to a lost signal). Figure 2.3 shows the data collected from a specimen with a 10mm long FBG embedded perpendicular to adjacent reinforcement fibers. Initially there is no loss of signal as can be seen in the first eight seconds in Figure 2.4a. This continues for the initial 5% of the cycles before data points are regularly lost. As can be seen in the Figure 2.4b, data points are successfully recorded during the lower loading (troughs) with a few exception, but are lost (and recorded as 0) intermittently during higher loading (peaks). The intermittent nature of the signal loss at later cycles can be attributed to the dynamically varying strain field

due to the formation of defects in the vicinity of the FBG sensor. Under certain combinations of uneven strain state, the FBG spectrum is split whereby the interrogation algorithm can no longer detect the Bragg wavelength, thus leading to intermittent data loss.
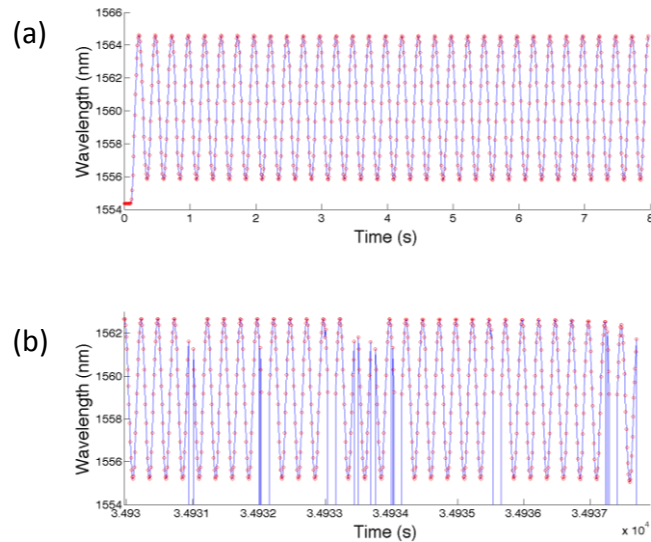
Figure 2.3: Cyclic variation of wavelength of 10mm long FBG: (a) initial eight seconds, and (b) final eight seconds.
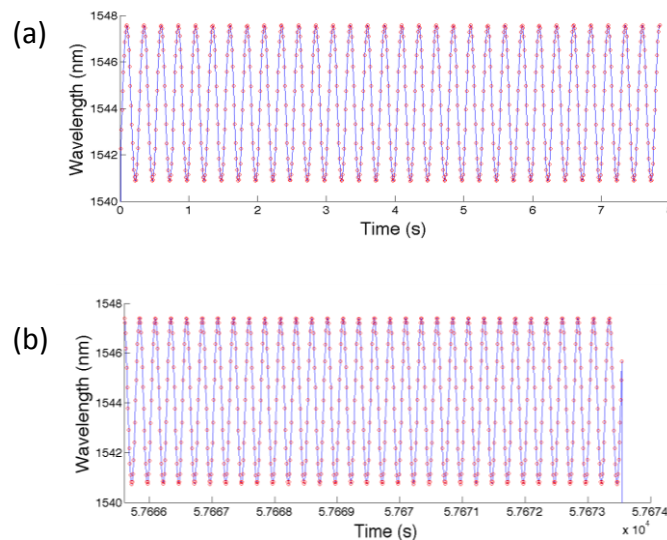
Figure 2.4: Cyclic variation of wavelength of 1mm long FBG: (a) initial eight seconds, and (b) final eight seconds.

Figure 2.4 shows the data collected from a specimen with a 1mm long FBG embedded in line with the reinforcement fiber. It can be seen that the data points are recorded at virtually every time step from the initial cycles (Figure 2.4a) up to failure (Figure 2.4b).

To further illustrate the reliability of 1 mm FBG sensor under high cycle fatigue experiment, the spectrum of the FBG sensor is recorded at different duration of experiment

(Figure 2.5). One may note that FBG sensor holds its integrity for the entire duration of the test and does not show any noticeable degradation or peak splitting, which clearly points out the reliability and accuracy of measurement for the entire duration of the test.
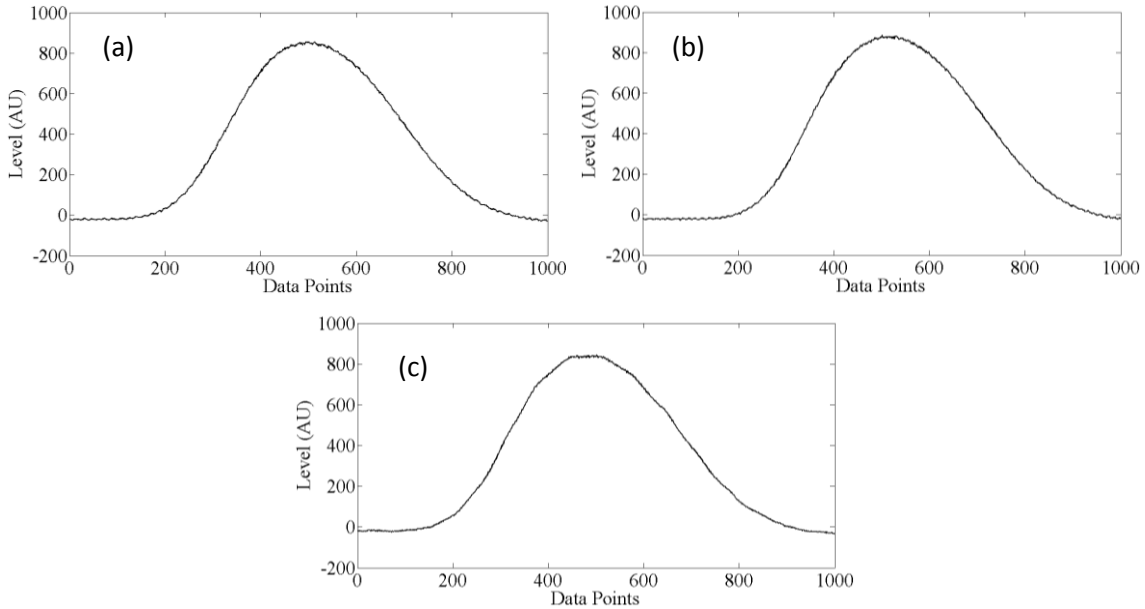
Figure 2.5: Spectrum of the 1 mm FBG sensor; (a) before the fatigue experiment has started, (b) at 3×10^6 cycles, and (c) at nearly 4×10^6 cycles.

After failure, the specimens were sectioned, polished and examined under a microscope. The density of matrix cracking was measured in order to correlate the effect of the crack spacing and FBG length.

(a) (b)

Figure 2.6: Microscopic images of cross section of specimens in loading directions. Transverse cracks just above the fiber optic cable (b) can be seen clearly. The cross section is taken along the fiber direction.

Figure 2.6 shows a cross section of the specimen after fatigue testing. A number of cracks can clearly be observed in the figure. The average crack density was measured to be

roughly 1.1mm. The interaction between the fiber optic and the composite was also inspected in order to determine if the FBG was debonding inside the laminate, which may be contributing to the loss of the signal. Figure 2.7 shows a cross section of the embedded fiber optic. It appears that there is no detrimental interaction between FBG and the composite and hence no debonding in between them. As one may note from this figure, the fiber optic sensor is surrounded by three different regions, namely, reinforcing fibers parallel (region 1) and perpendicular (region 2) to the fiber optic and matrix (region 3). This case might further contribute to the development of uneven strain distribution around the FBG. However, the sinusoidal wavelength change and the FBG spectrum data show that 1mm FBGs are not prone to uneven strain distribution which can normally cause peak splitting; hence they can easily provide local strain data reliably.
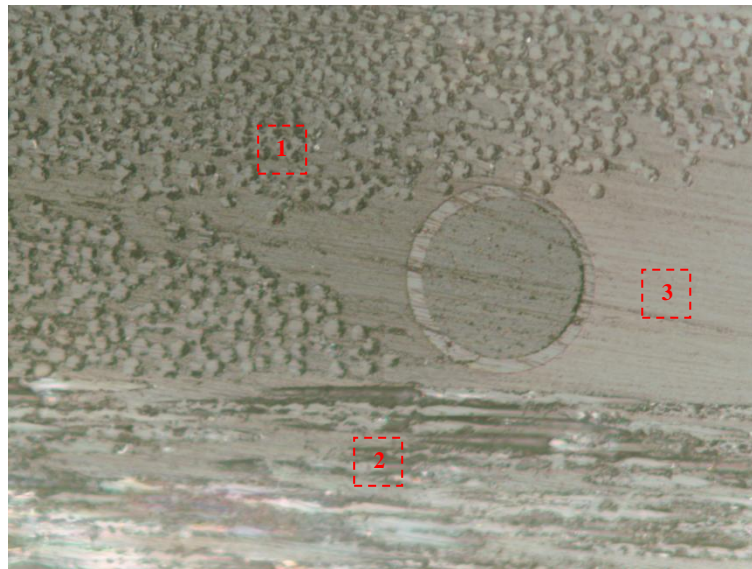
Figure 2.7: Microscopic image of cross section of embedded optical fiber.

The difficulty in embedding FBG sensors in composite materials having inherent local non uniform strain distributions lies in ensuring that sensors are under an even strain field. Three important main factors influence the consistency of the field thereby enabling FBGs to reliably monitor strain during fatigue loading. The first factor is the relationship between FBG length and tow width. In a composite made with non-crimp fiber (NCF) material, tows (bundles of fiber) are stitched together to make up a fabric. Once the composite is processed, the regions between the tows are resin rich compared to those regions within the tows. The stiffness of the resin rich areas is less than within the tow since there is only resin and no glass fiber to increase the stiffness. This results in an uneven strain field across a number of tows when a load is applied. In the material used in the study, the tow width is on the order of

2mm. This is greater than the length of the 1mm long FBGs and less than the length of 10mm FBGs. At most a 1mm long FBG will experience one resin rich area while a 10mm long FBG will experience four resin rich areas. The more excessive variation in strain seen in a longer FBG results in a broader reflection spectrum and in some cases causes a loss of the ability to track the peak wavelength. Figure 2.8 describes this configuration and shows the relative sizes of FBGs and tow width. In line with the concept of maintaining an even strain field by reducing the number of tows that cross an FBG, the reinforcement fiber orientation also plays an important role. If the fiber optic is embedded in-line with the reinforcements that it is in contact, it will experience a less uneven strain field. Figure 2.8 shows the two possible optical fiber/fiber reinforcement orientations. The experimental results show that optical fibers oriented in-line with the reinforcement (Figure 2.8b) had a sharper reflected spectrum and were therefore more reliable.
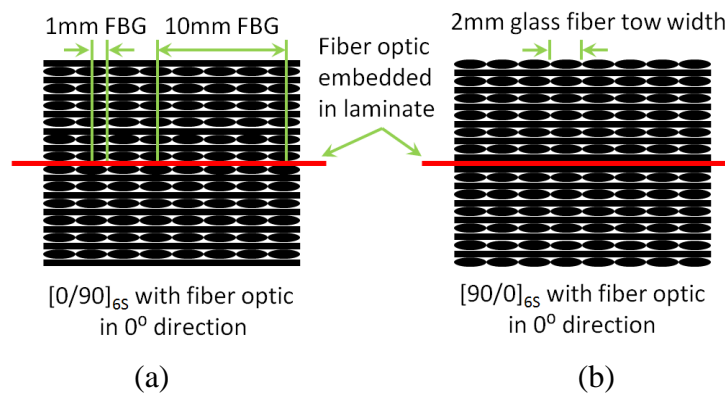
Figure 2.8: Schematics of embedded FBG.

The crack density plays a similar role to tow width in maintaining a consistent strain field. When a crack in the composite develops, the region around the crack experiences a different strain field than the intact composite. Thus, formation of multiple cracks in the vicinity of FBG can create uneven strain field along the sensor length. The crack density in our specimens that were examined under optical microscope is around 1.1mm. This is slightly larger than the 1mm long FBGs. On average, the 1mm long FBGs will experience one crack while the 10 mm long FBG could experience nine cracks leading to higher probability of exposure to such uneven strain fields. This reinforces the fact that the 1mm long FBGs produced better data than the 10mm long FBGs.

In addition to three main factors influencing the measured signal accuracy, namely; tow width to FBG length relationship, optical fiber and adjacent reinforcement fiber orientation and crack density resulting from fatigue loading, other factors such as edge

delamination, and composite thickness might also influence the measurement accuracy of the signal. The edge delamination is triggered by interlaminar stresses occurring in the proximity of free edges because of layer-wise difference in elastic properties. The current lamination structures are selected given its ease for manufacturability and also placing the FBG sensor perpendicular and parallel to tow directions achieved by the stacking sequences of $[(0/90)_6]_S$ and $[(90/0)_6]_S$, respectively. Out of these two stacking configurations, $[(90/0)_6]_S$ configuration is expected to carry smaller edge delamination risk than $[(0/90)_6]_S$. However, it should be born in mind that the regular distribution of interlocked layers can reduce the edge delamination hazard. In our experiments, we have not observed any edge delamination that can alter the signal behavior. Moreover, noting that the FBG sensors are positioned away from the free-edges, the edge effects if existing are not prominent to affect our measurements. If the FBG sensor is to be placed nearby the edges, possible occurrence of edge delamination should be considered, which can be reduced through optimizing the ply angles as elaborated in detail in [48]. Another important factor that needs to be taken into account might be the thickness of the laminate. If the laminate thickness is comparable to the diameter of the optic cable and thus the FBG sensor, the signal quality of the FBG sensor might be altered under the fatigue loading. It is noted that in our another work, 1 mm long FBG sensor embedded into the midplane of 2.26-2.21 mm thick symmetric composite laminates having six layers of either unidirectional glass (600 Tex, 283 gr/m^2) or carbon fibers(800 Tex 12K, 300 gr/m^2) gives reliable signal when subjected uniaxial static tensile loading. However, the fatigue behavior of short FBGs in thin laminate is not investigated within the scope this works and will be examined in our further studies.

2.4. Conclusions

When an FBG is under an uneven strain field, the reflected spectrum will broaden and eventually split into a number of peaks. This results in either a loss of signal or an inaccurate signal due to a peak shift caused by the split. To embed FBGs in an even strain field three factors should be kept in mind: i) tow width to FBG length relationship, ii) optical fiber and adjacent reinforcement fiber orientation, and iii) crack density resulting from fatigue loading. The tow width should be greater than the length of the FBG so that it only experiences one region of uneven strain (the resin rich area between the tows). The optical fiber should be aligned with the direction of the adjacent reinforcement fibers. This further reduces the

uneven strain field found between the tows. Ideally the crack density should be equal to or greater than the FBG length. Cracked regions have different strain level in the local vicinity compared to the intact region and therefore contribute to an uneven strain field in a similar manner to the resin rich regions between tows. Experimental results show that the signal from a 1mm long FBG embedded in-line with adjacent reinforcement fiber within a NCF material with tow widths of ~2mm, and a 1.1mm crack density after fatigue testing is much more reliable than a 10mm long FBG embedded perpendicular to adjacent tows.

CHAPTER   3

Investigation of Strain and Temperature Distribution in Fiber Reinforced Composites Subjected to High Strain Fatigue Loading Using Embedded FBG Optical Sensors

3.1. Introduction

In this research, performance and behavior of FBG sensors embedded inside glass reinforced composites are studied under constant high strain, low-cycle fatigue loading conditions in order to assess the mechanical energy, strain distribution and evolution along the composite specimens. Understanding FBG response under low-cycle fatigue conditions is important in terms of applicability of these sensors to monitor structures that are exposed to repetitive high dynamic loads. It is shown that strains from the sensors located in different locations can decrease and significantly deviate from each other as low-cycle fatigue progress notifying the distinction between the global and local response of the material. To the best of author's knowledge, there is no published research on investigation of sensor behavior for high strain fatigue of fiber reinforced composites. This work attempts to unravel the sensor response to detect the internal strain behavior under such loading conditions. It also aims to address the practical problems regarding the fatigue testing under constant displacement and strains utilizing different measurement devices of the testing system. Furthermore, using thermocouples, autogenous heating of the composite samples was also investigated to understand the temperature variations for fiber reinforced composites composed of biaxial glass fibers and epoxy matrix undergoing cyclic loading.

3.2. Experimental

3.2.1 Specimen preparation and testing equipment

In order to manufacture the composite plates, Resin Transfer Molding (RTM) and vacuum infusion (VI) methods were used. In the course of this study, 5 composite laminates were fabricated, and four of which were produced using RTM. The RTM method is particularly suitable for manufacturing of high quality, high volume fractions and near net-shape composite parts. Laboratory scale RTM apparatus which provides the ability of embedding optical fibers into the composite parts was used to produce flat panels with the dimensions of 620mm x 320mm x 3.5mm wherein optical sensors are embedded. Composite laminates consisted of E-glass fiber and epoxy resin and have the stacking sequence of $[90/0]_{6S}$. Metyx LT300 E10A 0/90 biaxial E-glass stitched fabric was used as the reinforcement, which has an area density of 161 g/m^2 in the 0° orientation, that is aligned along the resin flow direction in the mold, and 142 g/m^2 in the 90° orientation, leading to total of 313 g/m^2. The selected resin system is Araldite LY 564 epoxy resin mixed with XB 3403 hardener (manufactured by Huntsman Corporation) with the ratio of 100 and 36 parts by weight. The panels undergo an initial cure at 65 ^{o}C for 24 hours with a post cure at 80 ^{o}C for 24 hours. Three 1 mm long FBG sensors having the Bragg wavelengths of 1540, 1550 and 1560 nm that are written on the same fiber optic cable with 4 cm or 6 cm intervals were purchased from FiberLogix. Prior to manufacturing, fiber optic cable was fixed onto 0° surface of a ply through passing it under stitching fibers. The plies are stacked such that the fiber optic cable is between the 6th and 7th layers of the laminate as shown in Figure 3.1a. The composite panels are cut into mechanical test specimens using a water-cooled diamond circular blade saw, which have the final dimensions of 250 mm $\times$ 25 mm $\times$ 3.7 mm with a 150 mm gage length. The length of the specimen is aligned with the 0° fiber orientation. In the specimens with FBG sensors, the middle FBG (1550nm) was positioned at the center of the specimen's gage length and the remaining two sensors were located towards the grips. All three sensors were oriented along the loading direction. To avoid damage and in turn the breakage of test specimens at grip locations, both ends of specimens are tabbed with an aluminum tab having a dimension of 50 mm $\times$ 25 mm $\times$ 1mm using two-component room temperature curing epoxy system (Araldite 2011).

All tests were performed on an MTS 322 test frame with MTS 647 hydraulic wedge grips using an MTS FlexTest GT digital controller with MTS Station Manager software. Load and displacement data were collected with a built in load cell, (model: MTS 661.20F-03) and linear variable differential transformer (LVDT), respectively. Strain was collected with an axial extensometer, model: MTS 634.25F-24. Micron Optics SM230 interrogator with Micron

Optics Enlight software was used to collect the FBG data. K-type thermocouples are used to measure temperature and corresponding data was collected using a National Instruments NI SCXI-1314 DAQ card in a NI SCXI-1000 chassis with LabVIEW software. All data is acquired at a sampling rate of 100Hz.

(a)   **(b)**   **(c)**
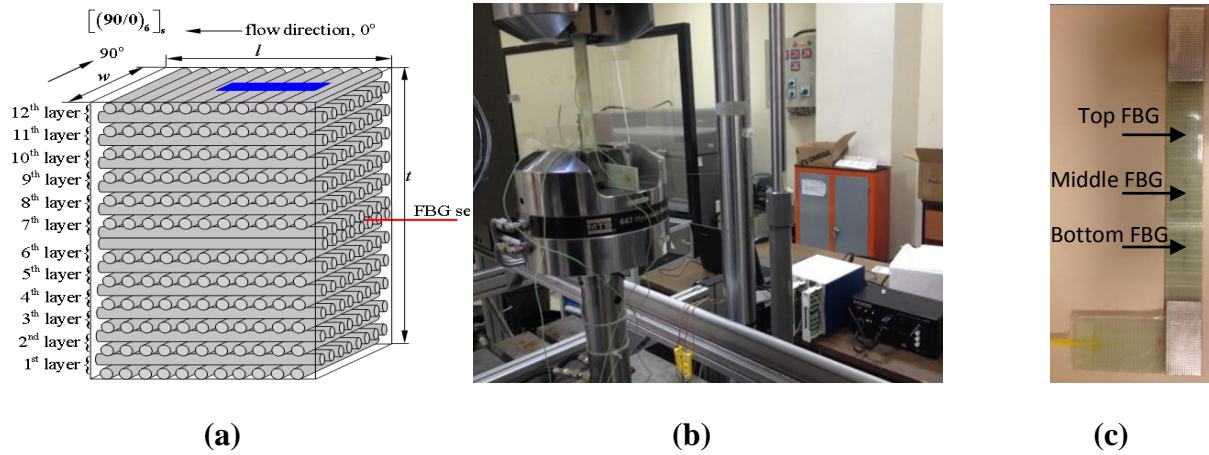
Figure 3.1: a) The schematic drawing for stacking sequences together with the placement of FBG sensor and also the orientation of the cut specimen indicated by blue region where l, w, and t indicate the length, width and the thickness of the manufactured composite plate, **b)** fatigue testing system and equipments, and **c)** L-shaped specimen that enables easy egress of the fiber optic cable.

3.2.2. Test procedure

In order to determine baseline parameters for fatigue tests, eleven static tests were performed whereby the average ultimate tensile stress and strain of the composite specimens were determined to be 320 MPa and 16.31 mε, respectively. In this study, six FBG embedded specimens are subjected to constant amplitude strain and tension-tension sine wave tests at various strain ratios ($\varepsilon_{max}/\varepsilon_{ult}$) varying between 0.5 to 0.6 where the maximum fatigue loading which needs to be imposed on these test specimens were determined based on the strain ratio of interest. To ensure that the fatigue tests for all specimens are performed in tension-tension mode, all specimens are subjected to   minimum stress of 27.6MPa. Autogeneous heating of the test specimens become a concern during fatigue testing of glass fiber reinforced composites as the heat is not as quickly transferred to the environment as it is with metallic materials. The fatigue properties of composites are especially sensitive to heat. Tests are performed at a frequency of 4 Hz.

For each fatigue specimen, the strain sensitivities of embedded FBG sensors are determined as follows: First, the minimum and maximum loads are calculated using minimum

and maximum stress and area of the specimen. The given specimen is statically tensioned up to the calculated maximum load, and reloaded down to the minimum load while acquiring the displacement data by LVDT, the strain data by extensometer and the Bragg wavelength by the optical interrogator. The loading and unloading procedure is applied second time. Then, all the collected data are processed such that the extensometer data corresponding to the second ramp are plotted as a function of pertinent Bragg wavelength for each FBG and LVDT and linear regression is used to determine strain calibration coefficients for FBG and LVDT sensors.

Prior to fatigue testing, the temperature sensitivity of the FBG sensors was determined in order to account for the temperature variation in the specimens due to autogeneous heating. To this end, FBG sensors were placed in an oven. The temperature in the oven were ramped from 30 ^{o}C up to 60 ^{o}C and allowed to soak at each 10 ^{o}C temperature increment for one hour before the temperature and wavelength were recorded. A plot of wavelength vs. temperature is constructed for each FBG and linear regression is used to extract an average temperature sensitivity of 0.010 nm / ^{o}C for the FBG sensors. Before fatigue tests, three thermocouples were fastened to the surface of the specimens such that each one is located just above one of the FBG sensors in order to monitor the temperature increase due to autogeneous heating in the vicinity of the corresponding FBG sensor. Then, the surface temperature data of each thermocouple were converted into the wavelength shift using the previously determined temperature sensitivity coefficient and later the wavelength changes due to the increase in temperature were subtracted from the corresponding FBG wavelength data at each data point. Here, it should be noted that the surface temperature may not be the same as that sensed by the embedded FBG; however, it provides temperature information very close to the exact values thereby allowing for higher accuracy in the measured strain.

In this study, to investigate the behavior of FBG sensors under different experimental conditions, two different experimental procedures were utilized, namely fatigue experiments with LVDT and extensometer control mode as tabulated in Table 1. Four of the six fatigue experiments are performed under LVDT control whereas the remaining two experiments are conducted under the extensometer control. For experiments with LVDT control, the given specimen is subjected to the constant displacement corresponding to the desired strain ratio through using the LVDT sensor of the fatigue testing system. Recall that the displacement recorded by the LVDT was related to the strain acquired by the extensometer through a calibration coefficient as described previously. Prior to fatigue experiments controlled by the LVDT sensor, the extensometer was dismounted from the specimens and the fatigue

experiments were performed between minimum and maximum displacements imposed by LVDT. As for the experiments with extensometer control, the extensometer was mounted onto the specimens and kept thereon throughout fatigue tests. The specimens were strained between the minimum and maximum strains corresponding to desired strain ratios.

After fatigue test, the relevant sections of the broken fatigue specimens were cut into samples using circular saw blade to microscopically study the interaction between FBG and host composite material. Their pertinent surfaces are polished using different grits of abrasive papers and inspected under optical microscope and a Leo Supra 35VP Field Emission Scanning Electron Microscope (SEM).

Table 3.1: Test parameters for fatigue experiments.

Specimen Code	Strain Ratio	Fatigue Method
L1	0.61	LVDT
L2	0.6	LVDT
L3	0.545	LVDT
L4	0.6	LVDT
E1	0.57	Extensometer
E2	0.506	Extensometer

3.3. Results and Discussion

Data acquired from sensors throughout the fatigue tests of specimens are processed and presented as temperature, maximum strains at one cycle and mechanical energy variations as a function of cycle numbers in Figures 3.2-3.6. Here it should be noted that for all of the specimens, the intervals between the subsequent sensors are 4 cm except for the specimen E1 for which it is 6 cm. Figure 3.2a shows the variation of surface temperatures of the specimen L1 at three different locations as well as the ambient temperature, which were recorded with a K-type thermocouple with the sampling rate of 100 Hz. Here, it should be mentioned in passing that due to an unexpected error in data acquisition, data from FBG sensors and thermocouples were recorded only for initial 17000 cycles. However, the current data are still descriptive in terms of the fatigue behavior of the specimen at the pertinent strain ratio. The temperature of the fatigue specimen changes due to the mechanical work done on the composite. As can clearly be seen from Figure 3.2a, the temperatures recorded from the surface of the specimen steadily increase during very early cycles of the fatigue test due to the

autogeneous heating that occurs and then level off due to the fact that the rate of heat generation is compensated by the rate of heat transfer to the environment. Recall that the stiffness degradation of fiber reinforced polymer matrix composites experiences three different stages in response to cyclic loads. In Stage I, the rapid formation and interconnection of matrix cracking causes a sharp, and non-linear decrease in stiffness for the first 15-25 % of fatigue life. Initial rapid increase in temperature corresponds to this first stage of the fatigue life, followed by temperature settlement where Stage II of the fatigue life takes place. The observable difference in the values of temperature at different thermocouple locations might be attributed local differences in the damage formation across the length of the fatigue specimen. One may arguably state that the region having a larger increase in temperature might correspond to that with higher density of micro damage in the composite structure.
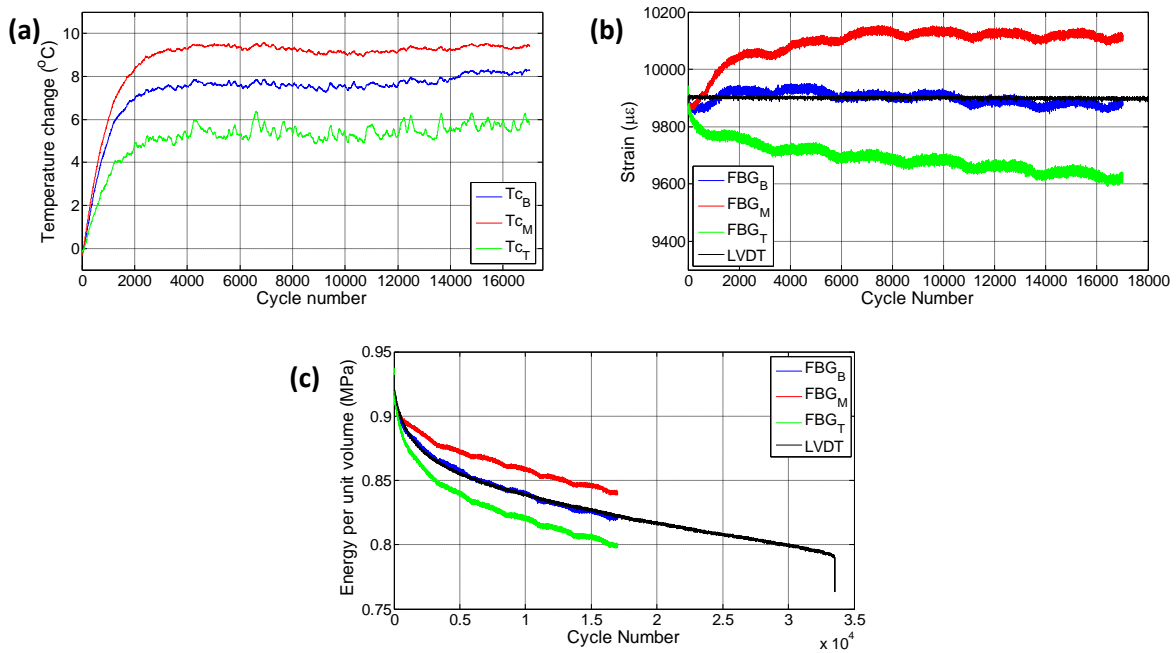
Figure 3.2: Evolution of temperature (a), strain (b) and mechanical energy (c) for all of the thermocouples and FBG sensors for the first specimen, L1.

Figure 3.2b shows the variations of maximum strains (i.e., peak strains in the sinusoidal strain form) that are recorded by LVDT and FBG sensors. Recalling that the fatigue on this specimen was conducted under constant displacement using the LVDT sensor, one may at first sight expect that FBG sensors should also give constant strain values. However, maximum strains gathered from the FBGs can be significantly distinct from the global behavior of the specimen. Different sections of the specimens can possess different strain variations during the loading process as inherent heterogeneity of the composite structure causes non-uniform strain distributions and elongations along the specimen

gagelength [49]. Another finding of this experiment is that the strain measured at different locations by the FBG sensors can significantly be different from each other as fatigue loading continues (i.e. between top and middle FBG sensors) thereby demonstrating reality of the non-uniform strain distribution due to the local difference in the damage form, density and evolution along the specimen gage length. Specimen L1 has failed at a location 1 cm above the lower grip close to the bottom FBG sensor.

To be able to scrutinize the possible relation between the strain evolution and mechanical strain energy (previously stated to have three distinct region during the entire fatigue experiment), in Figure 3.2c is plotted the mechanical strain energy per unit volume ($u=0.5\sigma_{max}\varepsilon_{max}$) as a function of cycle number. One can clearly notice that LVDT strain based mechanical energy possesses three distinct phases as discussed in the introduction section. Here, the initial sharp decrease corresponds to the first phase where the formation and interconnection of matrix cracking occurs rapidly. The second phase is characterized by the gradual linear decrease in mechanical energy due to the crack propagations, fiber debonding and delamination while at the third or final stage, the sudden drop in the mechanical energy is due to the fiber breakage. As the strains acquired from FBG and LVDT sensors differ, so do their corresponding energies and FBG sensors experience sharper decrease in their respective mechanical energies with respect to the one based on LVDT. It is interesting to note that the variation of strain as a function of cycle number for bottom and top FBG sensors in Figure 3.2b resembles to that of strain energy in terms of having initial sudden drop followed by the linear region.

To be able to repeat the previous experiment and acquire the FBG sensor data all through the fatigue experiment, specimen L2 was manufactured and subjected to the fatigue loading. For this test, processed temperature, maximum strain and mechanical energy variations are given in Figure 3.3.

(c)
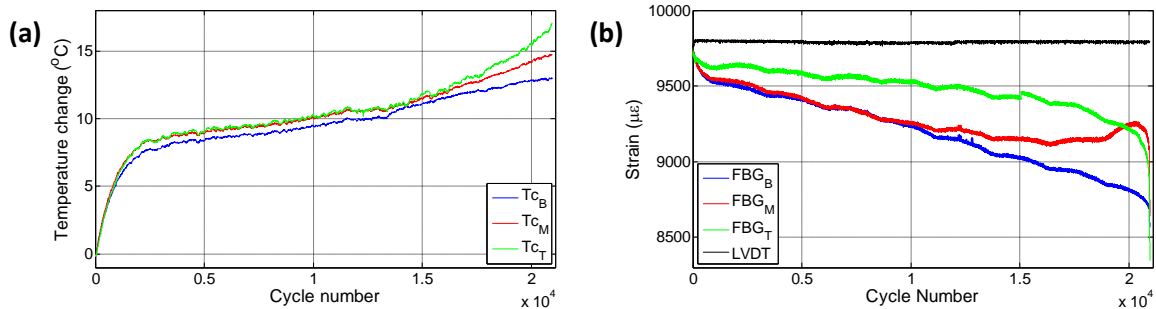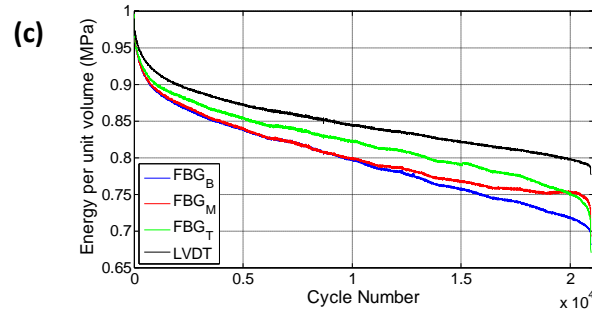
Figure 3.3: Evolution of temperature (a), strain (b) and mechanical energy (c) for all of the thermocouples and FBG sensors for the first specimen, L2.

Figure 3.3a presents the evolutions of temperatures for three different thermocouples. As in the case of the previous experiment on the specimen L1, there is also a rapid initial increase in temperature, which is followed by a region where the temperature rise is linear. Unlike Figure 3.2a, in this experiment, the temperature values of different regions are more close to each other, which might be due to the variability in the composite specimen and uniform damage formation along the specimen. There are two contributing factors that alter the temperature of the fatigue specimen, namely the autogeneous heating due to mechanical work on the system, and the friction between crack surfaces. In our relevant earlier work, it was shown that after the initial rise in the temperature, there is a gradual decrease in the temperature, which was followed by plato. This decrease is due to that the rate of heat generation is smaller than the rate of heat removal to the environment since as the damage is formed in the composite specimen, the force required to induce the desired strain drops whereby the mechanical work done on the specimen reduces, and also heat generation due to the friction between the deformation surfaces is not high enough to compensate heat removal. In Figure 3.3a, unlike our previous observation, there is no drop in temperature of the specimen which might be attributed to the fact that the damage being formed in the course of fatigue experiment is able to generate heat at a rate higher than the heat removal rate, therefore, the temperature of the specimens raises linearly, which might imply high damage density in the structure. Temperature rise occurs even though the mechanical energy applied onto the material drops associated to the decline in force due to the material deformation. At a later stage around 4000s, there is a noticeable deviation for the top thermocouple from the linear region such that the temperature rise is augmented. These three distinct regions are well correlating with the first, second and third phases of the energy curve. This suggests that while susceptible to external environmental effects, monitoring the surface temperature of composites subjected to fatigue may be used to give insight into the condition of the material.

Strain evolutions for the relevant sensors are provided in the Figure 3.3b. As in the case of results for L1 specimen, as the fatigue experiment progresses, the local strains measured by FBG sensors drop down such that the trend has a three distinct behavior, that is to say, initial sharp decrease followed by gradual nearly linear decline and finally sharp drop. Note that these three stages are in agreement with the previously stated fatigue phases observed in temperature and mechanical energy (based on LVDT) plots as a function of cycle number in Figure 3.3a and Figure 3.3c, respectively. This finding indicates that only strain monitoring with discrete embedded FBG sensors, one can conclude on the structural health of the composite specimen, which cannot be possible with strain gages due to the fact that under the fatigue loading, surface mounted strain gages experience debonding from the specimen surface and also lose their performance at later stages of the fatigue. Moreover, as before, the temperature is higher for the sensor with larger local strain. Globally, the specimen experiences a constant displacement/strain whereas there exist considerable differences in local strains measured from the sensors, which further increases as the test continues. Noting that as the fatigue experiment continues, the damage formed within the specimen causes permanent deformation and in turn elongation in the gage length of the specimen. Hence, it can be expected that the fatigue system should apply less force to induce the desired maximum displacement whereby the specimen effectively experiences less strain. As seen from the Figure 3.3b, the maximum strain values for the FBG sensors showed significant decreases in the strain values. Moreover, closer to failure, the strain of the middle FBG sensor starts to increase. This sudden change in the trend of the strain may signify the possible formation of major deformation other than fiber-matrix debonding and delamination alerting for the catastrophic failure before it can take place. This result is also consistent with the failure location of the specimen which occurred close to the middle FBG in the region between middle and top FBG sensors. The calculated mechanical energy using the strain data of all the respective sensors are provided in Figure 3.3c. Again, notable differences in the mechanical energy are present due to the fact that sensors sense different strain values. The comparison of Figure 3.2c and Figure 3.3c for the cycle number of 1.4×10^4 indicates that the specimen L2 involves more damage than L1 wherefore L1 specimen endured higher cycles number than L2.

The difference in the duration of the first phase detected based on FBG and extensometer/LVDT strain fields can be associated with the fact that the strain field of the sensor with larger gagelength such as extensometer and LVDT is affected by all the matrix

cracks along the gage length whereas the FBG strains are influenced by the cracks in the vicinity of the sensor having much shorter gagelength. Therefore, the first phase demarcated based on the FBG strain last shorter.

The third experiment was performed on the specimen L3 under displacement control with the strain ratio of 0.55 and was designed to consolidate the repeatability of the previous two experiments. Particular to this experiment, after 25000 cycles, the test was paused, the specimen was unloaded for 30 min, and then fatigue test was reinitiated while keeping the experimental conditions identical. Specimen has failed close to the middle FBG sensor in region between middle and top FBGs.
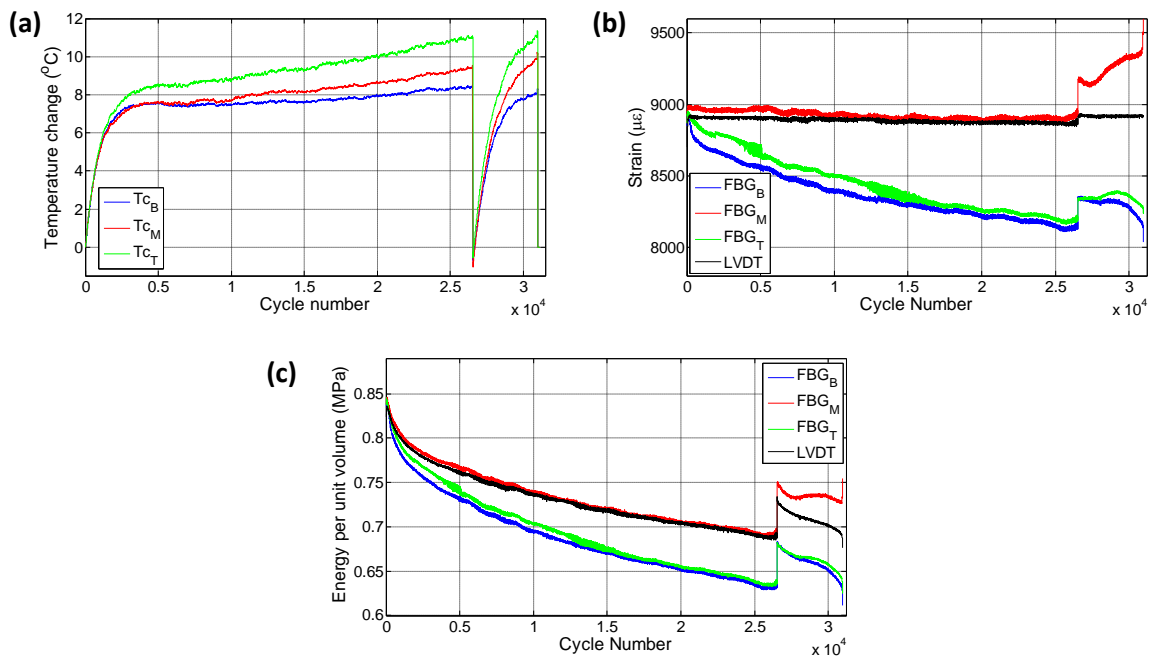
Figure 3.4: Evolution of temperature (a), strain (b) and mechanical(c) energy for all of the thermocouples and FBG sensors for the first specimen, L3.

Figure 3.4a presents variation of surface temperatures at three different thermocouple locations for specimen L3. For the first fatigue loading, similar to previous corresponding figures, the temperature at all three locations increase sharply and then follow gradual linear increase, which was stated to be corresponding to the second fatigue stage. Upon terminating the loading, all temperature values start to decrease as expected. A rather important observation that deserves some consideration is the temperature trend for secondary fatigue loading. Upon reinitiating the fatigue loading, it was noted that the rate of temperature rise was higher than that corresponding to the initial fatigue loading. The specimen temperature reaches the same values in a much shorter time, which can be attributed to the differences in the damage state of the specimen between the two cases. For the latter case, since the

specimen posses much higher damage and cracks distributed throughout the specimen, friction between the newly formed crack or damage surfaces lead to additional source of heat generation in the specimen, thereby increasing the temperature faster.

Corresponding strains and mechanical energies are given in Figures 3.4b and 3.4c. Again, strains have decreasing trend throughout the initial fatigue loading. When the fatigue loading was reinitiated again, maximum strains measured from the FBG sensors experienced sudden jump compared to the maximum strain of the last cycle belonging to the first fatigue loading even though applied maximum strain was kept same. The reason of such behavior can be attributed to the strain due the thermal expansion. It is seen that the specimen has a higher temperature at the end of the first fatigue loading than at the beginning of the second fatigue loading which implies that certain portion of the applied strain in the former case is contributed by the thermal strains associated to the thermal expansion of the specimen. When the specimens cools down and predefined displacement is applied again for the second fatigue loading, contribution from the thermal strain diminishes and more force is required to induce the desired displacement onto the specimen resulting in an upward jump in the measured force. This in turn influences the FBG strains along the specimen causing it to experience sudden increase.

After the jump in the strain, the maximum strains starts to drop down again until about 28000 cycles for all of the sensors. The rate of decreases in strain is significantly different compared to that corresponding to the end of the first fatigue loading for all the respective sensors. At this stage, the strains recorded by top and bottom FBG sensors continue to decrease whereas the strain of the middle FBG starts to increase pointing to significant deformations in the vicinity of the middle FBG sensor. After the restart of the fatigue test, specimen L3 withstands additional 6000 cycles of fatigue loading before the failure, leading to total of 31000 cycles to failure. Recall that the similar behavior was also noted for the middle FBG sensor of specimen L2. Both L2 and L3 specimens failed at a location close to the middle FBG in the upper part of the specimen (section above the middle FBG). The positions at which the specimens indicate the failed is consistent with the abrupt variations in the strain fields presented in both Figures 3.3b and 3.4b.

To further understand the outcomes of the initial 3 experiments, another specimen L4 is tested. Particular to this case, fatigue loading was imposed using LVDT control and extensometer was mounted onto the specimen to measure the strain during the fatigue loading. Similar to the specimen L3, two stage fatigue loadings were applied onto the

specimen. Initially, fatigue loading corresponding to the strain ratio of 0.6, was introduced for 15000 cycles and after around 30 minutes, second fatigue loading was applied with same maximum displacement loadings until failure resulting in an additional 4694 cycles to failure. Figure 3.5 shows the results for the strains and temperatures measured from different sensor systems and mechanical energy variations. Temperature variations of the specimens showed similar behavior as in the case of specimen L3 possessing distinct phases corresponding to the fatigue stages. At first initial rapid increase is detected followed by gradual increase in temperature. Top thermocouple showed the highest temperature variation. Consistent with the results of specimen L3, rate of temperature rise during the second loading was higher compared to the first fatigue loading as the friction between the crack surfaces formed during the first loading generates additional heat for the second loading. Upon analysis of the strain variations for the respective sensors, application of constant displacement onto the specimen causes decline in the strains measured from different sensors, extensometer can experience around 300 $\mu\varepsilon$ decrease in the measured strain. Such a reduction can be attributed to the elongation in the specimen causing less strain transferred to the specimen region within the gagelength of the extensometer in response to the same imposed global displacement. Another observation important observation is that decline of maximum FBG strains is higher compared to the extensometer strains. Such a behavior can be attributed to the damage formed in the surrounding regions of the FBG sensors as they can hinder the strain transferred between the reinforcing fibers and the FBG sensor causing acquisition of less strain. Again consistent with the previous results, strains measured from different FBG sensors showed different strain quantities due to the non-uniform elongations and damage formation along the specimen. At the second fatigue loading FBG strains behaved rather differently compared to the initial loading and closer to the failure there is a significant variation in the measured strain pointing out to the subsequent catastrophic failure. Specimen has failed at a location 2 cm above the lower grip and 1.5 cm away from the bottom FBG sensor. Maximum strains acquired from the bottom FBG sensor significantly increased at the last 1000 cycle of the fatigue loading signifying the occurrence of significant deformations in the vicinity of the sensor. Moreover, there is a sudden jump in strain upon application of the second fatigue loading which is due to the jump in the measured force. This Figure 3.5c illustrates the mechanical energy variations along the specimen for different sensor systems. There is synchronization between the phases of the temperature and mechanical energy variations in terms of time.
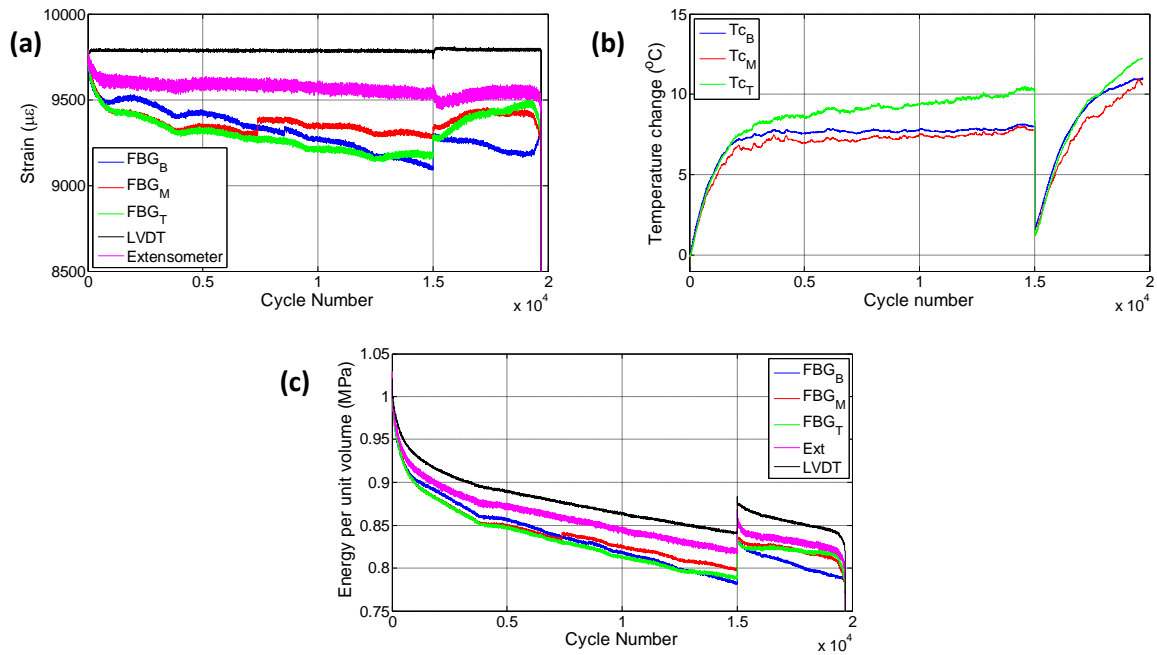
Figure 3.5: Evolution of temperature (a), strain (b) and mechanical(c) energy for all of the thermocouples and FBG sensors for the first specimen, L4.

To be able to shed a further light on the phenomenon as to descent in the maximum strains measured by the FBG sensors in the course of the fatigue loading, two additional experiments were performed under constant strain through using an extensometer mounted on the specimens until the failure where the pertinent specimens are denoted with E1, and E2. Similar to the results obtained from experiments with LVDT displacement control, the decrease in the maximum strain values are also noted for both E1 and E2 wherein FBG strains experience distinctive phases during the fatigue loading process. Experimental results for the specimen E1 are provided in Figure 3.6. For this specimen, the imposed strain ratio for the fatigue loading was 0.55. Particular to this specimen, the interval between the subsequent FBG sensors is 6 cm. Specimen failure from the grip location close to the bottom FBG sensor. Figure 3.6a yields local temperature variations along the specimen and in the environment. Here, the temperatures of all three locations increase sharply due to the autogenous heating, then gradually drop due to the fact that the specimen is being deformed and in turn less force is required to induce the prescribed displacement causing lower mechanical energy imposed around that region. This results in a level off since the rate of heat generation is balanced by the rate of heat transfer to the environment, and finally start to increase owing to the fact that the friction between the surfaces of micro cracks or damage acts as additional heat source within the specimen. Temperature variations for specimen E1 has rather good correlation with the three fatigue phases especially for the top thermocouple. Strain variations for the

respective FBG sensors and LVDT are provided in Figure 3.6b. Recall that using the previously determined calibration coefficient, the LVDT recorded displacement was converted into strain value. As can be seen from Figure 3.6b, until nearly 15000 cycles, the strain values of both extensometer and the LVDT are nearly the same. After this, the LVDT strain starts to increase drastically indicating significant deformation or elongation in the specimen to impose the desired strain onto the gage length region of the extensometer (50 mm). The similar trends in FBG recorded maximum strains are observed for the E1 specimen as well. Closer to the failure, that is to say, around 16000th cycle, the strain acquired by the bottom FBG sensor begins to reveal a sharper decline with respect to the other FBG sensor, which coincides with the onset of sudden increase in the LVDT strain. This can be attributed to the formation of major damages and elongations in the vicinity of the bottom FBG sensor alerting for the initiation of the third phase and catastrophic failure which is again consistent with the failure location which occurred at the lower grip from the tab section. Similar behavior is detected for the bottom FBG sensor of the specimen L4 where failure took place in the similar section of the specimen. For this experiment, the strain trends of the FBG sensors in Figure 3.6b follow the style of the mechanical energy variation calculated based on the constant strain recorded by the extensometer shown in Figure 3.6c.
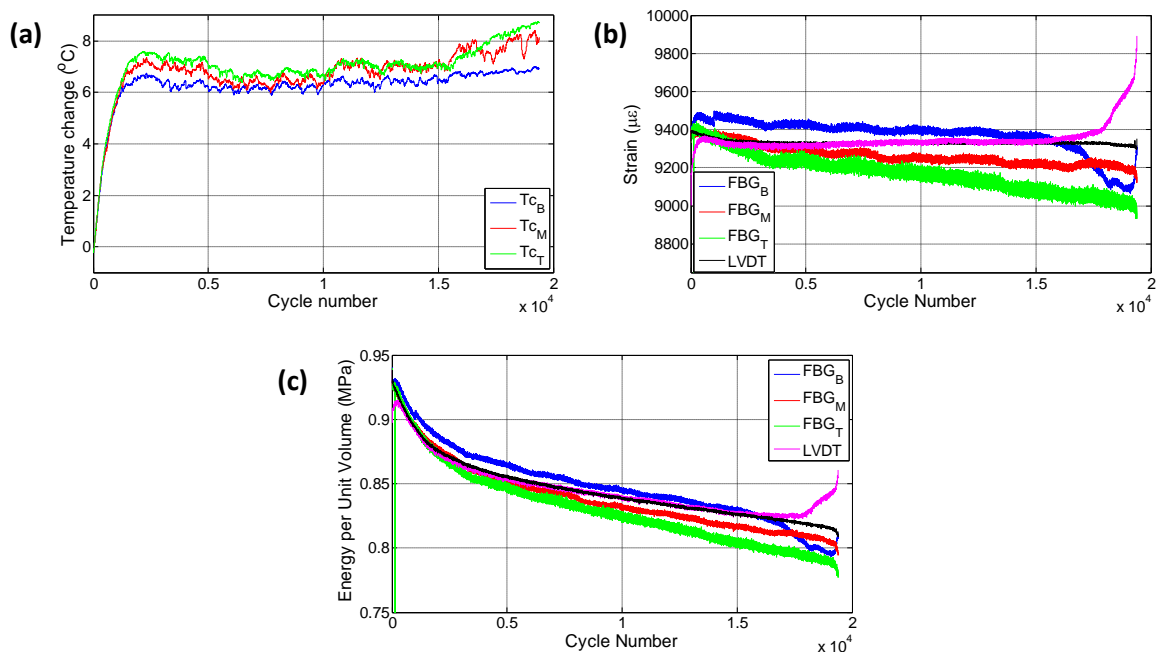

Figure 3.6: Evolution of temperature (a), strain (b) and mechanical(c) energy for all of the thermocouples and FBG sensors for the first specimen, E1.

Recall that the specimen E2, the last specimen of the present work, is manufactured by using VI method, and tested under extensometer control with the strain ratio of 0.5. Unlike

RTM specimens, this specimen was broken at a smaller cycle number, which might be attributed to one sided rough surface due to presence of peel ply, known to be the source of crack initiation points, or unnoticed possible defects which might have been caused during the manufacturing. However, the life time of the specimen is irrelevant within the focus of this study. In this test, in order to have further information on the strain variations along the specimen, a second extensometer with a smaller gage length was mounted onto the middle section of the specimen between the two ends of the first extensometer which inputs the strain data into fatigue testing machine) as shown in Figure 3.7. The results of this experiment are presented in Figure 3.8. Specimen has failed at a location between bottom and top FBG sensors as shown in Figure 3.10b. Temperature evolution on the surface of the specimen is given in Figure 3.8a, which has significant resemblances with previous experiments as expected. The second extensometer follows the first extensometer in the strain until the ten thousand cycles, and thereafter, shows deviation from constant strain value of the first extensometer, showing the importance of the gage length and the locality of the strain measurement in the specimen experiencing non uniform deformation, which is the case particularly for composite materials. In similitude with previous results, FBG recorded strains showed decrease over the length of the fatigue experiment. In this experiment, the third phase is rather distinctive in comparison to previous experiments such that there are abrupt changes and considerable decline in the all FBG measured strains as well as in the strain recorded by the second extensometer.
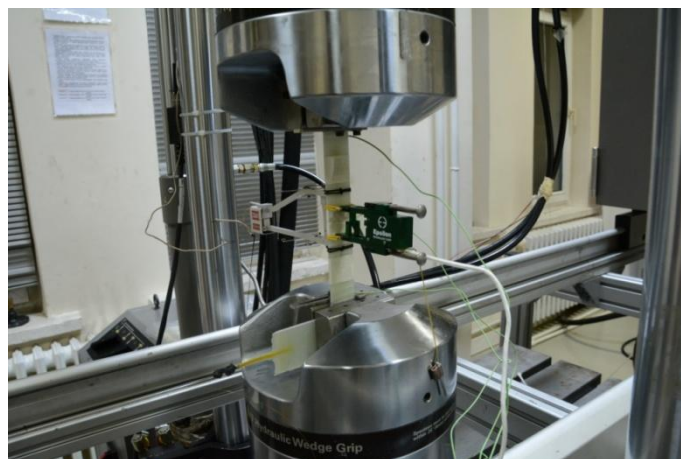
Figure 3.7: Additional extensometer was mounted for specimen
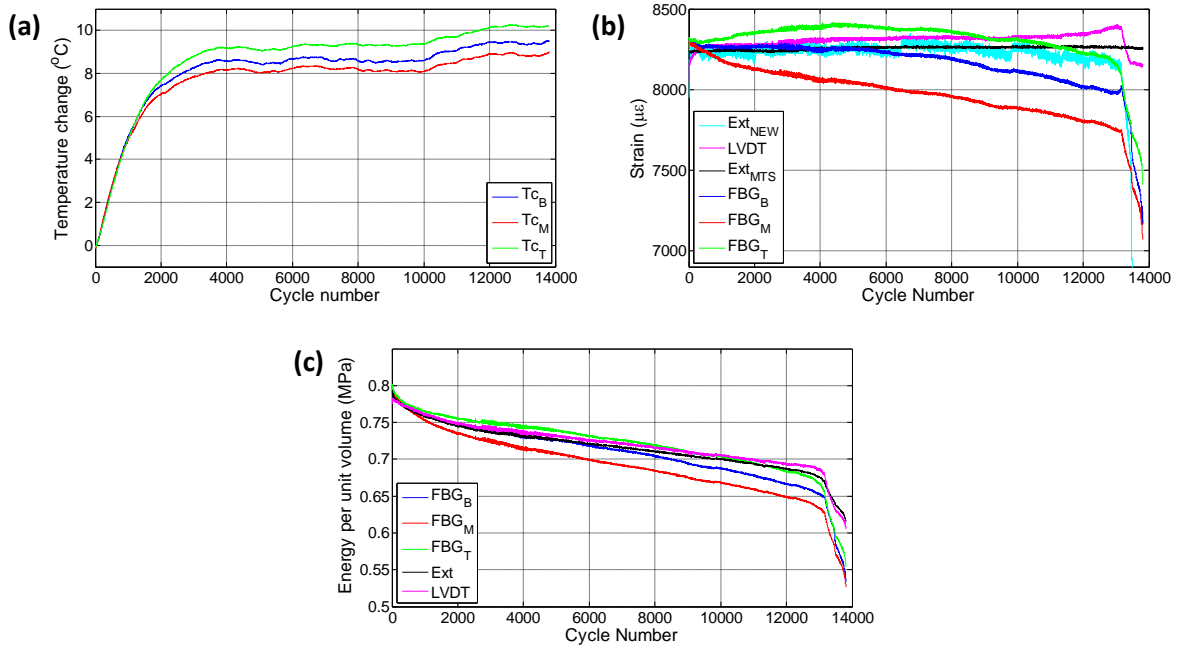
Figure 3.8: Evolution of temperature (a), strain (b) and mechanical(c) energy for all of the thermocouples and FBG sensors for the first specimen, E2.

Upon the analysis of the results acquired from the FBG sensors referring to strains fields recorded by LVDT and extensometers, it has been demonstrated that under constant amplitude, high strain fatigue loadings, the maximum local strains sensed by the 1 mm long FBG sensors can significantly be different from the global strain values measured over a larger gage length, and nearly in all experiments, FBG recorded strains decline. In addition, FBG sensors at different locations posses different strain fields attributed to the non-uniform strain fields or deformation states in discrete regions of the specimen.

At first sight, one may argue that this decline might be associated with the interaction between the composite and the FBG sensor due to the debonding of the sensing part of the FBGs and the deterioration of the FBG sensors. In order to examine the integrity of the sensor and its bonding with the host material, the cross sections of the composite specimens are inspected under optical microscopy and scanning electron microscopy and no noticeable debonding is detected as can be seen in Figure 3.9, which presents the cross section taken from the specimen L3.
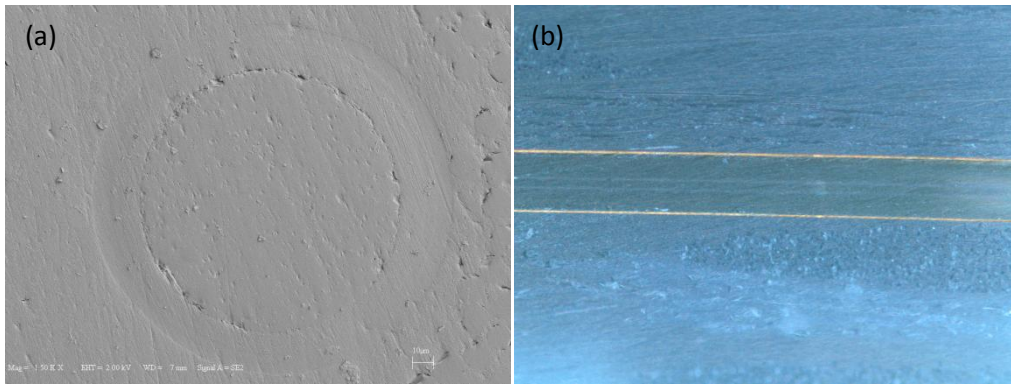
Figure 3.9: Perpendicular (a) and longitudinal (b) cross sections of optical fibers around FBG regions.

The formation of fatigue damages such as matrix cracking, fiber-matrix debonding and fiber breakages around FBG sensors can cause strain relaxations in the sensor region whereby FBG sensors may read significantly different strain from the globally applied one on the specimen. During the fabrication of composites specimen in this study, recall that FBG sensors have been placed parallel to 0° fibers within the symmetry axis of the laminate. Although the FBG sensors were placed in close contact to reinforcing glass fibers, they might be partially surrounded by resin rich regions as shown in Figure 3.10. Hence, the matrix will have an influence on the strain state in the vicinity of the FBG sensor owing to the matrix cracking due to the applied loads. Cracks formed within the reinforcing fiber tows can also contribute to this process. Also, possible reinforcing fiber-matrix debonding may lessen transfer of the globally applied strain onto the FBG sensor. Moreover, the fiber breakage in the composite can considerably alter the structural integrity thereby causing profound local variations in the strain field. The progressive damage modes in the fatigue experiments are well captured by the FBG sensors such that the variation of strains recorded by FBG sensors can follow the three fatigue phases of the composite corresponding to different damage mechanisms. In the light of all experimental findings, it is believed that the strain relaxation in vicinity of FBG sensors is one of the contributing reasons for the observed reduction in the maximum strains measured by FBG sensors. Thus, FBG sensors can provide valuable information regarding the strain and damage state of the internal regions in the specimen.
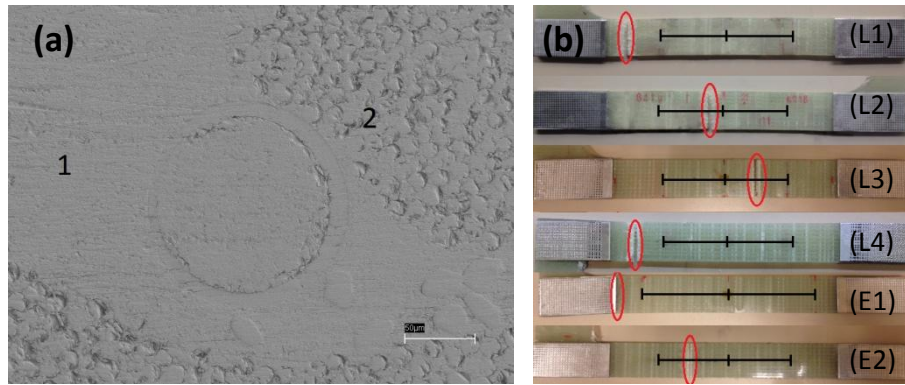
**Figure 3.10:** a) Cross section of FBG sensor; region 1 shows the resin rich areas that the fibers are in contact and region 2 represents the longitudinal fibers parallel to the sensor where fiber-matrix debonding can be observed, b) Failed specimens, failure locations are marked with the red circles and sensor locations are indicated with black vertical tics.

The strain distribution as sensed by the FBG sensors within the specimen subjected to fatigue loading may vary appreciably and the variation can be more profound as the cycle number increases, which can be prudently attributed the nonlinear strains that the specimen experiences due to the heterogeneity in its structure and the formation of different damage states. Moreover, closer to the failure of the specimen, at least one of the FBG sensors shows notable divergence in the maximum strain, notifying the initiation of the third phase of fatigue life of composite and subsequent catastrophic failure in parallel with the failure location of the specimen. Although, the constant displacement/strain were applied to the composite specimens, FBG sensors show distinctive maximum strain behavior capturing the fatigue phases of the composite material rather than showing constant and uniform strain fields.

Furthermore, another crucial point that requires attention is the gage length of the dynamic extensometer used for the fatigue testing. Extensometer measures the strains within its gage length i.e. the region between its pins and fatigue testing system impose constant strains only along this region. As a result, the remaining parts of the 150 cm gage length towards the grip sections can show very distinct strain behavior from the middle part of the specimen. It should also be pointed out that the FBG sensors located at the center of the gage length experience decrease in the strain even though they are located within the extensometer gage length for which the global strain is set to be constant. Thus, local and global strain values can differ significantly from each other and FBG sensor experiences the local strain that is reduced or enhanced by the formation of defects.

One can deduce from the temperature trends that during the initial stages, shows rapid increase and reaches a steady state condition where rate of increase settles or there is reduction in the temperature. This trend can be followed by a temperature rise closer to the

failure of the specimen. Such distinct regions signify the three phases of the composite undergoing fatigue loading. First rise in the temperature corresponds to the first phase where rapid crack formation and interconnection occurs. As heat transfer settles between the material and the environment and crack formation rate decreases, materials enters into the second phase where debonding and delamination is the dominant damage mechanism. Initiation of the higher rate of increase closer to the failure signifies the third phase where catastrophic failures take place. Similar temperature variations was also observed for woven laminates undergoing fatigue loading in the literature with parallel damage mechanisms associated to the related fatigue stages [50]. In this work, transition cycles and related durations associated to the different stages in temperature tend to follow the stages related to the mechanical energy variations.

In one of our previous studies [31], FBG embedded composite specimens with the same constituent materials as in the case of this study were subjected to a constant strain high cycle fatigue loading (i.e., with the strain rations of 0.27, and 0.4). It was observed that the maximum strains of the FBG sensors did not experience severe decline compared to the results of the present work, suggesting that under smaller strain ratios, the deformation is more limited and uniform in time.

3.4. Conclusions

Composite specimens containing three subsequent FBG sensors embedded along their gagelength are exposed to constant, high strain fatigue loads. Considerable discrepancy occurs between the individual sensors and external sensors i.e. LVDT and extensometer as the loading continues demonstrating the significant difference between the local and global behavior of the material. It is found that fibers that are exposed to same global strain condition did not necessarily give rise to the same strains at the local level. It is demonstrated that such response from the FBG sensors can be attributed to the heterogeneous structure of the material causing nonlinear strain distribution and relaxation of the strain in the sensor vicinity due to the formation of various damage mechanisms such as matrix cracking and fiber-matrix debonding. This causes sensor strains to follow a certain trend with different stages similar to the stages in stiffness or mechanical energy degradation. Sensor gagelength is a crucial factor to consider as constant strains imposed using an extensometer does not necessarily induce similar strains over other strain sensors. Moreover, temperature variations in response to fatigue loading also show distinct stages and they are contributed by the mechanical energy input and the friction

between the surfaces of the newly formed deformations and cracks. Upon application of the second fatigue loading as in the case of specimen L3 and L4, temperature rises to the same temperature quantities in a much shorter time compared to the first fatigue loading revealing the contribution of the friction between the crack surfaces to the generation of heat.

CHAPTER 4

The Performance of Embedded Fiber Bragg Grating Sensors for Monitoring Failure Modes of Foam Cored Sandwich Structures under Flexural Loads

4.1. Introduction

In this work, failure modes of foam core sandwich sandwich composites are investigated by evaluating three different failure modes using embedded Fiber Bragg Grating (FBG) sensors. Sandwich specimens with FBG sensors embedded inside their composite facing were manufactured using vacuum infusion and later, subjected to static and cyclic loading conditions under 3-point bending mode. Formation of different failure types are tracked utilizing the wavelength shift and spectrum information acquired from the sensors in order to understand the sensor behavior. Exploiting how sensors respond to a particular damage mode, failure detection strategy is developed for damage characterization to achieve reliable structural health monitoring of sandwich structures.

The understanding of the strain evolution induced by flexural loading and the response of sensor to different damage states in sandwich composites is crucial in terms of applicability of these sensors into real structures. To this end, this work aims to improve the current understanding on the behavior of embedded FBG sensor in foam cored sandwich composites through investigating the performance of FBG sensors for detecting different failure modes and in turn establishing damage detection strategies which are very important for the safe usage of these materials in a variety of service conditions.

4.2. Experimental Procedure

In order to assess the applicability of FBG sensors for monitoring different failure modes such as facing indentation, compressive facing failure, and core shear failure, sandwich

composites with different facing and core materials are manufactured and processed into test specimens with and without FBG sensors using circular saw blade. Before testing the FBG embedded specimens, three to four samples without FBG sensors are cut from each sandwich plates and then tested mechanically under three-point bending with crosshead speed of 3mm/min in order to determine the required experimental conditions for the FBG integrated samples. For all bending tests, the span length of specimen is chosen to be 200 mm. Ten FBG embedded specimens are tested, the experimental results are analyzed, and three of the test results with FBG sensor are rejected due to experimental procedure error related to either manufacturing or mechanical testing. For each sandwich type, FBG sensors are embedded between the first and second fabric layers just above the core. It should be stated that in the course of this work, we have used both 1 mm and 10 mm long FBG sensors. 1mm long FBG sensors are used for the accurate acquisition of strain and its evolution during the test while 10 mm long FBG sensors are utilized to monitor damage formation (indicating itself as nonlinear/complex strains) through tracking the response of the reflected spectrum as well as the wavelength shift. All FBG sensors are either embedded just below or 20 mm away from the loading point to investigate the detection capability of the sensors as a function of distance. Sandwich composites are manufactured using PVC structural core materials (Airex and Gurit) with the density and thickness of 80 kg/m^3, 10mm and 200 kg/m^3, 8mm, respectively. Unidirectional and 0/90 biaxial E-glass stitched fabric (METYX) is used as facing reinforcement. The area densities of the fabrics are 300 g/m^2 for UD glass fiber and 302 g/m^2 for the 0/90 biaxial glass fiber with 161 g/m^2 in the 0° orientation, which is aligned along the length of the specimen and 141 g/m^2 in the 90° orientation. The sandwich structure is impregnated by epoxy resin system (prepared by mixing Huntsman LY564 epoxy and XB3403 hardener with weight ratio of 100:36) using vacuum infusion process as shown in Figure 1 and then cured at 70^oC for 20 hours. To assure that the embedded FBG sensors do maintain their intended placement without sliding during the handling and manufacturing process, the FBG written optical cable is interlaced through the stitches of the reinforcement of first fabric layer. Table 4.1 tabulates the configuration of five different sandwich structures whose results are presented and discussed in forthcoming sections referring to associated failure modes.
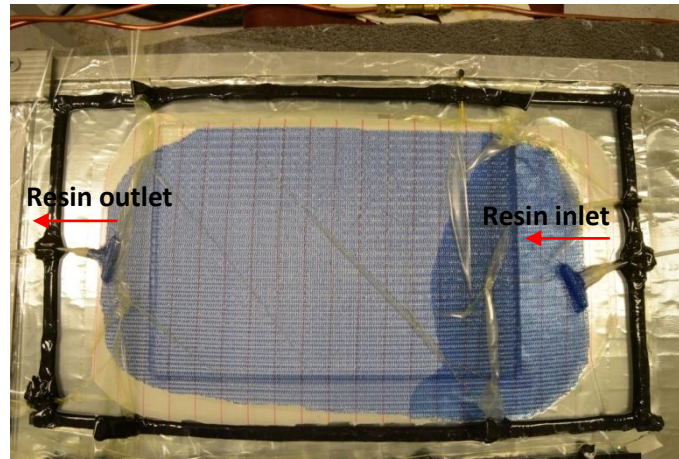
Figure 4.1: Experimental set-up for manufacturing sandwich plates using vacuum infusion process.

Table 4.1: Configuration of manufactured sandwich composites with glass fiber (GF) facing.

Specimen Code	Facing Material	Core thickness [mm]	Core density [kg/m3]	Stacking Sequence	FBG Length [mm]
SWC1	2x Biaxial	10	80	$[90/0/\{FBG\}0/90/c]_s$	10
SWC2	4x UD	10	80	$[0_3/\{FBG\}0/c]_s$	10
SWC3	6x UD	10	80	$[0_5/\{FBG\}0/c]_s$	10
SWC4	4x UD	10	80	$[0_3/\{FBG\}0/c]_s$	1
SWC5	4x UD	8	200	$[0_3/\{FBG\}0/c]_s$	1
SWC6	4x UD	8	200	$[0_3/\{FBG\}0/c]_s$	10
SWC7	4x UD	8	200	$[0_3/\{FBG\}0/c]_s$	10

In the course of performing static three-point bending tests on samples without FBG to determine baseline mechanical properties, it is observed that the core of the specimen crushes prematurely and in turn fails at the point where the load is applied from upper support due to the load concentration. To circumvent this problem, a glass fiber tab is placed under the upper support to diminish the concentrated load in accordance with the ASTM standard [51].

The first four specimens with FBG sensors in Table 1 are dedicated to study the effect of facing material on the local indentation failure. For specimens named SWC1, SWC2 and SWC4, FBG sensors are positioned such that they are just below the loading support of the 3-point bending apparatus within the compressive facing. A 10 mm long FBG sensor is embedded in SWC1 and SWC 2 to detect the structural changes occurring below the loading point through particularly monitoring the reflected spectrum. As for SWC4 specimen, two 1 mm long FBG sensors are embedded in the structure, one of which is located in the upper

facing while the second FBG sensor is positioned in the lower facing, to evaluate the strain and damage evolution both in tensile and compressive side of the sandwich specimen. SWC3 contains 10 mm long FBG sensors positioned 20mm away from the loading point within the compressive facing in order to screen the deformation, scrutinize behavior of spectrum change upon loading and assess how the distance of the sensor to the failure location effects its response qualitatively. For the remaining specimens SWC5, SWC6 and SWC7, FBG sensors are embedded into the compressive facing such that they are positioned 20mm away from the loading support. SWC5 specimen is integrated with 1 mm long FBG sensor to study the compressive failure of the facing through monitoring the evolution of the strain. SWC6 and SWC7 specimen is used to investigate the core shear failure damage mode by capturing delamination and related strain releases based on both the reflected spectrum and wavelength information acquired from the sensor. In order to find strain sensitivity of the FBG sensors, strain gages are patched onto the compressive facing surface at a distance of 20 mm from the loading point. Assuming linear strain distribution along the thickness and the span length, the strain at the FBG sensor location is determined by linear interpolation of the strain measured by the strain gage. Subsequently, the wavelength shift is plotted as function of interpolated corresponding strain whereby the gage factor for the FBG sensors is found. This procedure is applied for several specimens and average sensitivity of 1.25 pm/$\mu\varepsilon$ is found. FBG sensors are interrogated with a Micron Optics SM230 interrogator at a rate of 100Hz.

Using the baseline properties (i.e., yield point, and corresponding standard travel) of specimens without FBG sensors, sandwich beams with FBG sensors are tested under both static and cyclic loading in three-point bending mode in order to investigate the sensor response and damage formation. Initially, the bending load is applied onto the specimens until reaching the standard travel of 2 mm with the crosshead speed of 5mm/min. This standard travel position is chosen such that it is well below the yield point of the sandwich specimen so that no permanent damage is inflicted thereon. Having had a standard travel of 2mm, the crosshead is returned to its initial position and then, the specimen is subjected to cyclic flexural loads with crosshead speed of 10mm/min. For the cyclic tests on all specimens, 1mm standard travel is utilized as the minimum displacement and maximum standard travel is varied for each specimen to impose different degrees of damage on the specimens. After the completion of cyclic loading, the specimen is unloaded, and then is subjected to first static flexural load corresponding to 2mm standard travel whereby it becomes possible to compare the response of the FBG sensor under the same loading condition for intact and damaged states where the damage is induced as a result of the cyclic loading. Wavelength and spectral

response of the FBG are recorded and results are discussed succinctly in the following section. The accumulation of damage in consequence of the cyclic loading is quantified through using a damage parameter, D, defined in Eq.3 [45, 52]. The modulus for each cycle is evaluated using the facing stress calculated by using Eq. 2 [36] and the strain measured utilizing the FBG sensor.

$$\sigma_x(x) = \pm Px / 2b(h_c + h_f)h_f \quad 0 \le x \le L/2, \tag{2}$$

where σ_x is the stress, P is the applied load, b is the width, and h_c and h_f are thickness of the core and facing, respectively. Here, x represents the distance from the end support of the 3-point bending apparatus and is equal to $L/2$ just below the loading point. Depending on if the facing side is exposed to compressive or tension loads, the stress can be negative and positive, respectively.

$$D_i = 1 - E_i / E_o, \tag{3}$$

where D_i is the damage parameter for the ith cycle, E_i is the flexural modulus at ith cycle and E_o is the initial flexural modulus.
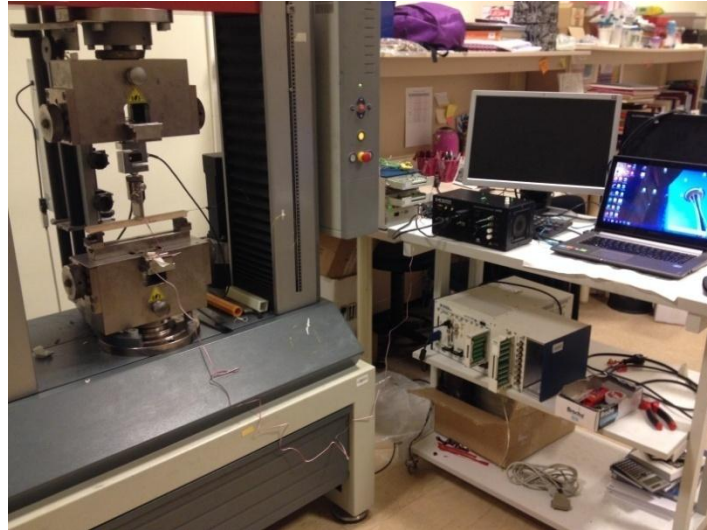

Figure 4.2: Test setup for the sandwich specimens

4.3. Results and Discussion

In this section, we have discussed experimental results of seven FBG embedded specimens in terms of strain measured by FBG sensors, spectrum response, and damage parameter to be able to illustrate the efficacy of embedded FBG sensors for monitor different

failure modes. For the first 4 specimens given in Table 4.1, it is noted that due to the low density of the core, the sandwich specimens are crushed locally just below the loading point. The indentation of the core results in a loss of structural integrity at earlier stages of the cycling loading without fully exploiting the facing performance, hence leading to the same failure mode for all three specimens. For specimens SWC5, SWC6 and SWC7, core material with higher density is employed, which provides enhanced resistance to compressive loads through the thickness and hence, is less prone to associated premature core crushing. Compressive failure of the facing and core shear failure are the damage modes studied using specimens SWC5, SWC6 and SWC7.

Static and cyclic test results of SWC1 are given in Figures 4.3- 4.6. For the cyclic loading of SWC1, the maximum load corresponds to the standard travel of roughly 5.2 mm as seen in Figure 4.3. Upon approaching the standard travel of 5.2 mm, permanent deformation starts forming since this point is above the yield point of the sandwich beam. At this level, as can be seen at the first cycle in Figure 4.4, the compressive strain recorded by the FBG sensor falls notably due to the core crushing causing the FBG sensor to read less compressive strain. On the removal of the load, significant amount of residual strain (i.e., 344 $\mu\varepsilon$) is measured by the optical sensor.
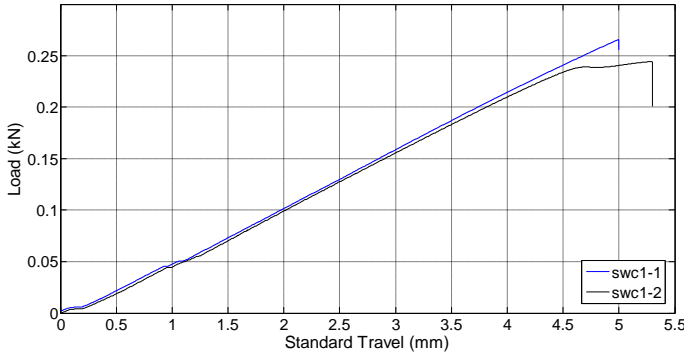

**Figure 4.3**: Static test results of SWC1 specimens without FBG.
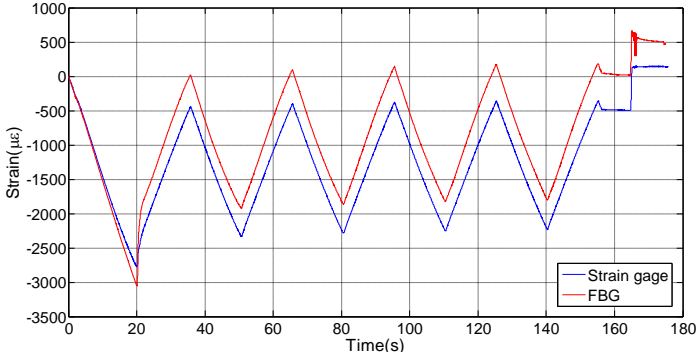
Figure 4.4: Strain responses of strain gages and FBG sensor under the cyclic loading.
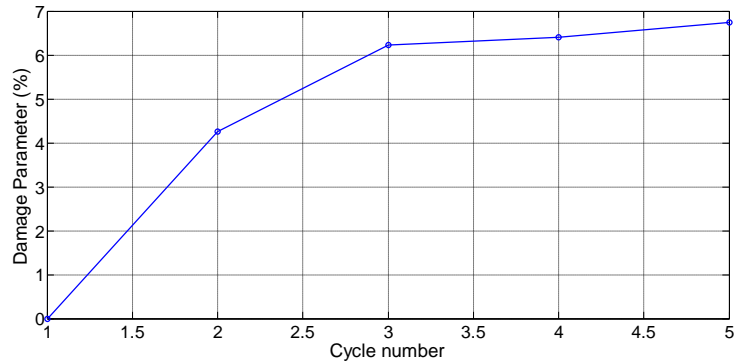
Figure 4.5: Damage parameter evolution for SWC1 during cyclic loading

In order to quantify the damage accumulation, damage parameter is calculated and then plotted with respect to cycle number as shown in Figure 4.5. Since the sandwich specimen experiences permanent deformation during the first loading cycle, the damage parameter significantly increases indicating the severity of deformation during the initial cycle. The rate of damage accumulation decreases since the material experiences lower degree of plastic deformation as the cyclic loading continues and it reaches steady state after the fifth cycle number. Figure 4.6 yields the spectrum response of the FBG sensor before, during and after the cycling loading from which one may note that the spectrum splits into multiple peaks, pointing to the occurrence of complex/non uniform strain states due to the damage formed in the vicinity where the FBG sensor is embedded (in this case, the upper face sheet of the sandwich specimen). Figure 4.6c further shows that the damage on the specimen is permanent since after the removal of the cyclic load on the specimen, the spectrum splitting is retained. The peak splitting is owing to damage induced compressive strain in the transverse direction, which causes elliptic fiber cross section whereby the optical fiber carries multiple wavelength modes related to the polarization of the light. In this particular case, the permanent deformation is associated with the local facing indentation leading to permanent bending of the facing and hence the fiber optic sensor as shown in Figure 4.7.
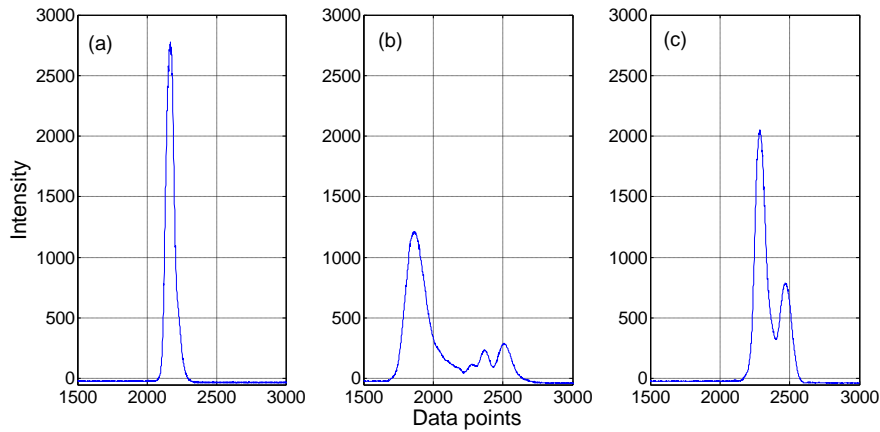
Figure 4.6: The spectrum response of FBG, a) before cyclic loading, b) during cyclic loading (around 120 s after the start of the loading), and c) after the cyclic loading.
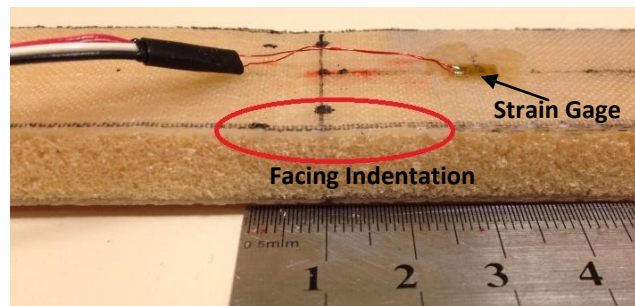
Figure 4.7: Permanent indentation of the upper facing after the tests. FBG is located beneath the srain gage.

Further tests are carried out to supplement the results of SWC1 testing. To this end, specimen SWC2 is exposed to same testing procedure and results are provided in Figures 4.8-4.10. FBG sensor is located just below the loading support. This time maximum standard travel of 5mm was applied for the cyclic loading.
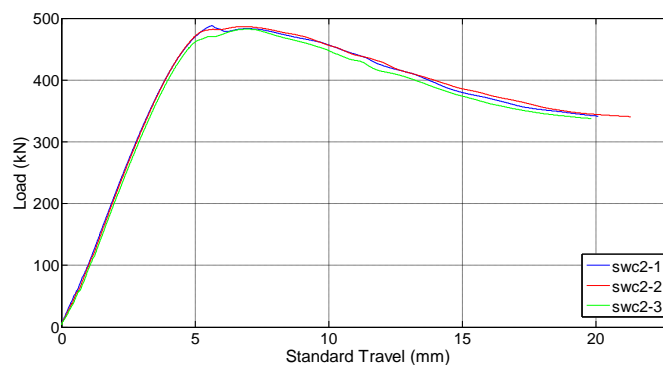
Figure 4.8: Static test results of SWC2 specimens without FBG.
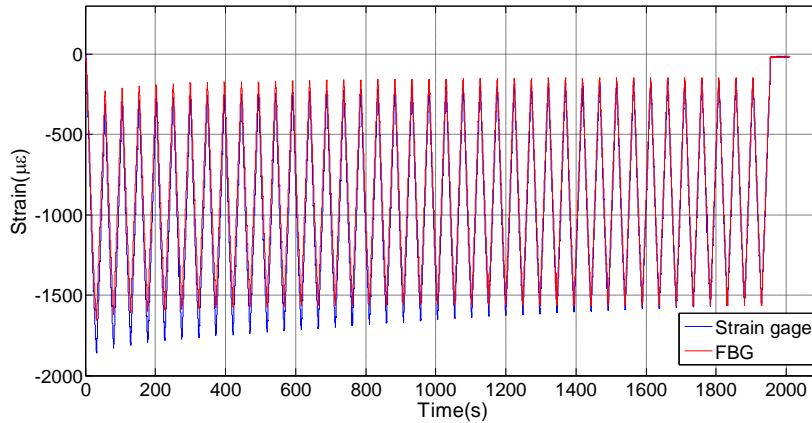
Figure 4.9: Strain responses of the cyclic loading, measured by a strain gage and FBG sensor.
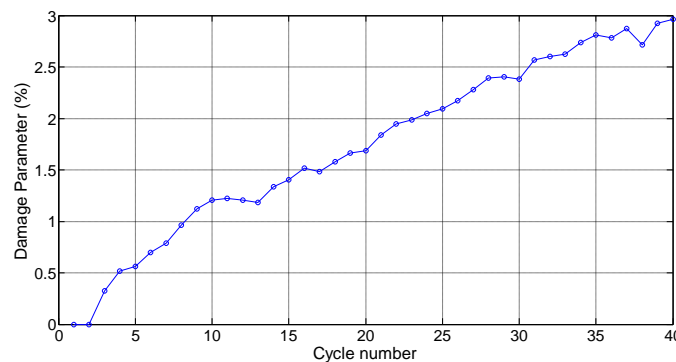
Figure 4.10: Damage parameter evolution for SWC2 during cyclic loading

As 5mm standard travel is around the yield point of the material, damage accumulation tends to increase as the cyclic loading continues without reaching a steady state condition. Since the yield point is close, cyclic loads can induce plastic deformations over longer cycle range and accumulates the associated damage without leveling of even after 40 cycles. Lower damage quantities are achieved compared to the specimen SWC1, as maximum displacement was lower and facing material of the specimen is more durable. Moreover, as the sensor region is more intact and has not experienced imminent strain relaxation similar to the SWC1, no significant reflected spectrum distortion was detected during the cyclic loading. After the completion of the cyclic loading, specimen is subjected to static loads until major reduction in strength is observed inducing significant further facing indentation. Strain variations of both FBG and the strain gage are provided in Figure 4.11. After around 65s, strain gage starts to sense tensile strains as the deformation gets more severe. However, FBG sensor continues to sense compressive strains demonstrating the disperancy between the internal and surface strains. Failure mode and significant residual strain (178 με) was detected by the FBG sensor after the removal of the load. Associated reflected spectrum variation is provided in Figure 4.6. As non-uniform strain fields form during the loading

process, spectrum can be significantly distorted (Figure 4.6b). As the static loading induces much severe deformation onto the specimen, after the removal of the load, peak splitting is observed as in the case of SWC1 (Figure 4.6c).
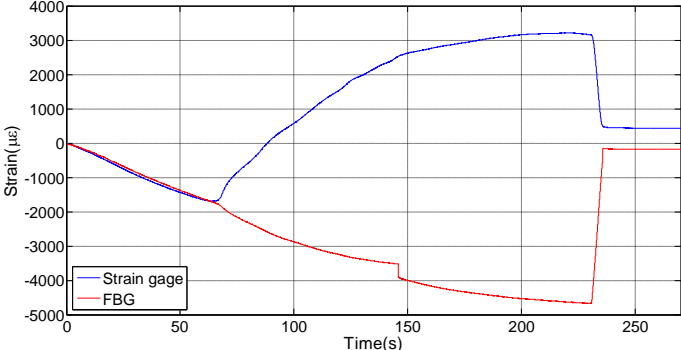
Figure 4.11: Strain evolution for static loading until failure.
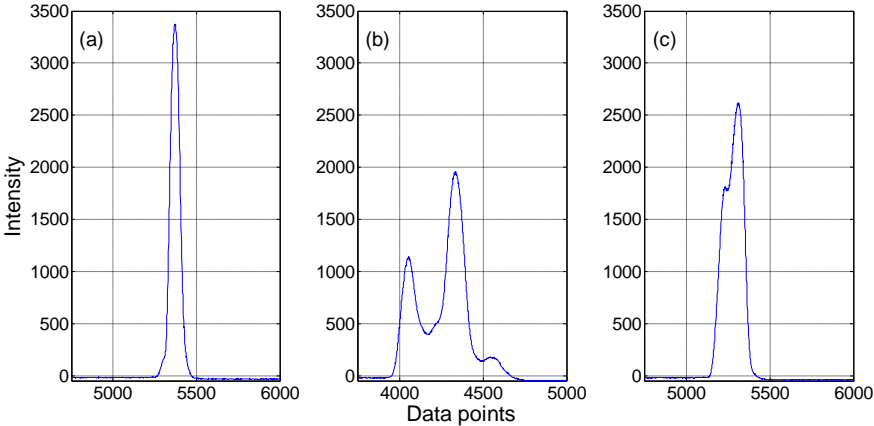
Figure 4.12: The spectrum response of FBG, a) before loading, b) during static loading (around 200 s after the start of the loading), and c) after the loading.

For specimen SWC3, results of static and cyclic three-point flexural tests are given in Figures 4.13- 4.15. Cyclic loading is applied such that the maximum standard travel reaches 3.5mm. As the cyclic loading continues, the deformation within the specimen accumulates and in turn, maximum and minimum strains measured in each cycle decreases as observed in Figure 4.14. As the strain gage is located in the surface, it experiences higher bending that the FBG sensors which is located beneath the sensor within the facing. This causes strain gage to measure higher compressive strains than the FBG.
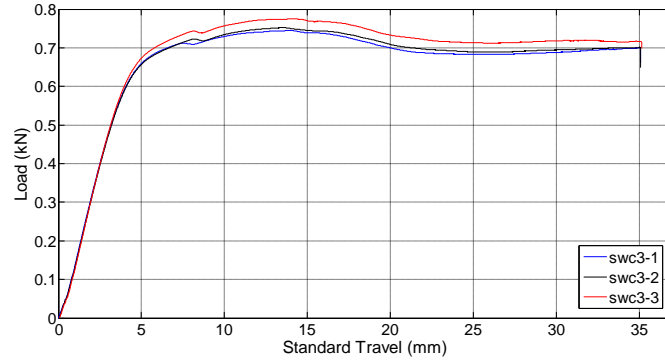
Figure 4.13: Static test results of SWC3 specimens without FBG.
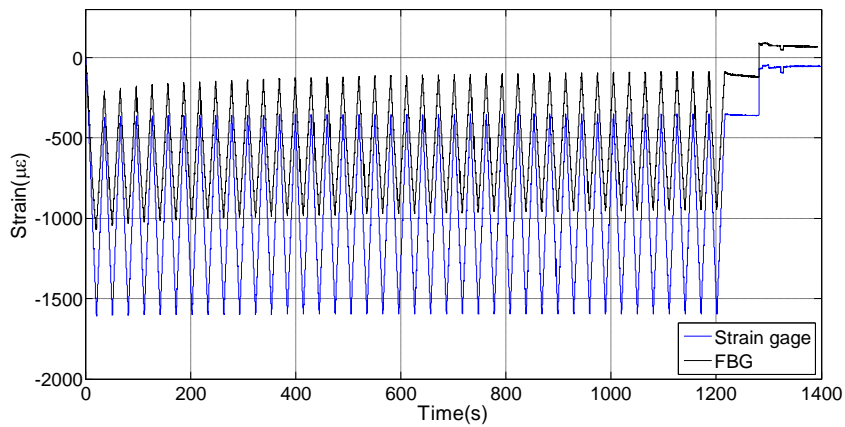
Figure 4.14: Strain responses of the cyclic loading, measured by a strain gage and FBG sensor.
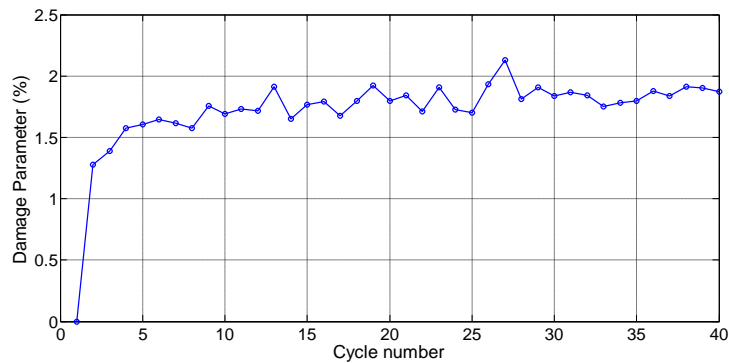
Figure 4.15: Damage parameter evolution for SWC2 during cyclic loading

Here, it should be noted that the damage parameter for SWC3 is smaller than that for SWC1 and SWC2 since the maximum standard travel imposed on SWC3 is much below the yield point of the sandwich specimen and the FBG sensor is located 20 mm away from the loading point. As clearly seen in Figure 4.15, the damage parameter exhibits initial sharp increase as in the case of SWC1, followed by gradual rise as the cyclic loading continues. Nearly after 27 cycles, the damage accumulation levels off at a value of 1.8, indicating that the applied load can longer induce further plastic deformation on the specimen. The damage type for SWC3 is closely related to the facing indentation and core crushing formed due to the

continual application of cyclic loads. As in the case of SWC2, having completed the application of the cyclic loading, the specimen SWC3 is loaded until the failure corresponding to the standard travel of 15 mm such that the core is totally crushed. The failure mode observed in the specimen is enhanced core crushing and subsequent facing indentation immediately below the loading point. As can be seen in Figure 4.16, the FBG sensor starts to measure tensile strains rather than compressive strains after 150 seconds, which can be attributed to the fact that the sensor region experiences higher degree of bending deformation causing the sensor region to be stretched thereby leading to tensile strain fields therein. Figure 4.17 indicates the evolution of the FBG spectrum in the course of the static loading (after the completion of the cyclic test). The non-uniform strain states created during the static loading cause the reflected spectrum to broaden and split. However, after the failure and the subsequent removal of the load, the spectrum shows single peak since the uneven/transverse compressive strain fields diminish. Although the spectrum recovers its original shape with single peak, there is noticeable broadening of the spectrum (Figure 4.17f) compared to the initial state (Figure 4.17a), signifying the presence of non-uniform strains in the vicinity of the FBG sensor. Accordingly, considerable amount of irreversible deformation associated with the facing indentation results in a residual strain of 2400 $\mu\varepsilon$ recorded by the FBG sensor after the failure. Here, it is noted that the strain gage measures compressive strains throughout the test which is like a mirror image of FBG recorded strain after roughly 75 seconds. This difference points out that the interior of the material can experience rather distinct strain states than its surface. Depending on the heterogeneity of the composite structure, tensile strain fields can be formed within the interior of the facing after considerable bending of the specimen causing FBG to sense positive strains.
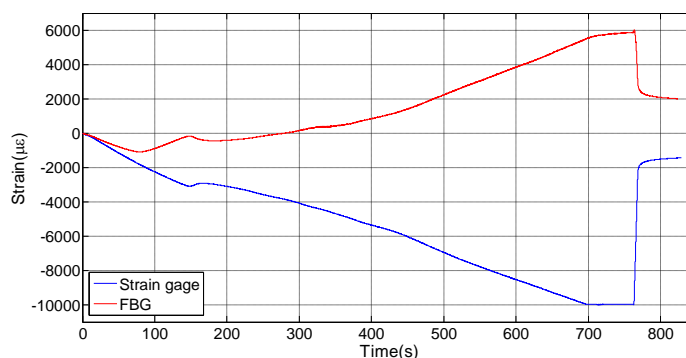
Figure 4.16: Strain evolution for static loading until failure.
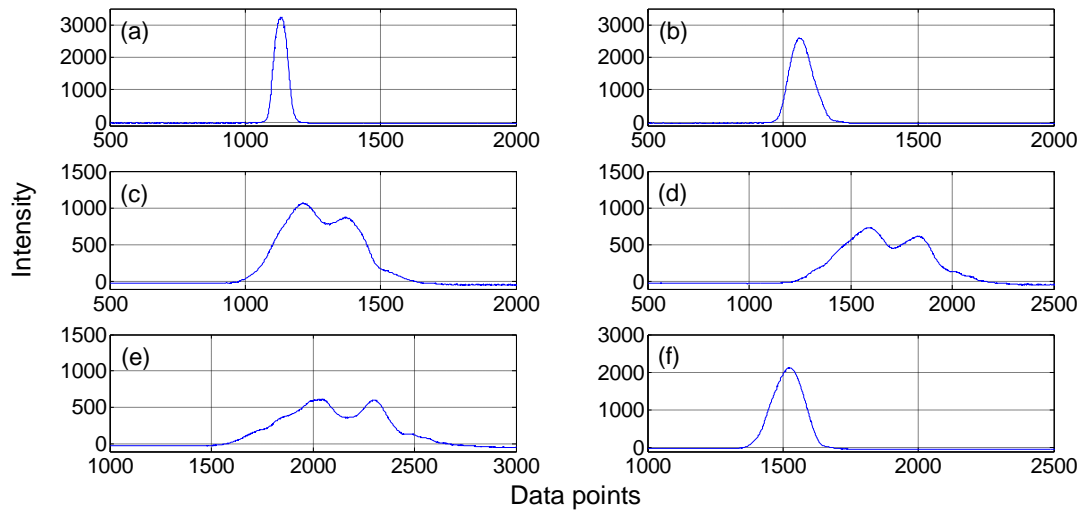
Figure 4.17: FBG spectrum response evolution for static loading until failure, a) before loading, b) around 240s, c) 378s, d) 516s, e) 654s, and f) 792s after the application of the loading.

Figure 4.18 shows load versus standard travel curve for the static flexural tests of SWC4 specimens without embedded FBG sensors while Figure 4.19 illustrates the strain acquired by the FBG sensor under the cyclic loading with the maximum standard travel of 4mm, which is way below the yield point of the specimen as seen in Figure 4.18.
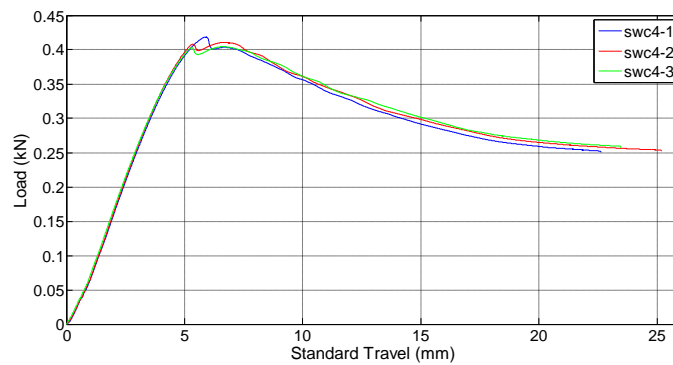
Figure 4.18: Static test results of SWC4 specimens without FBG
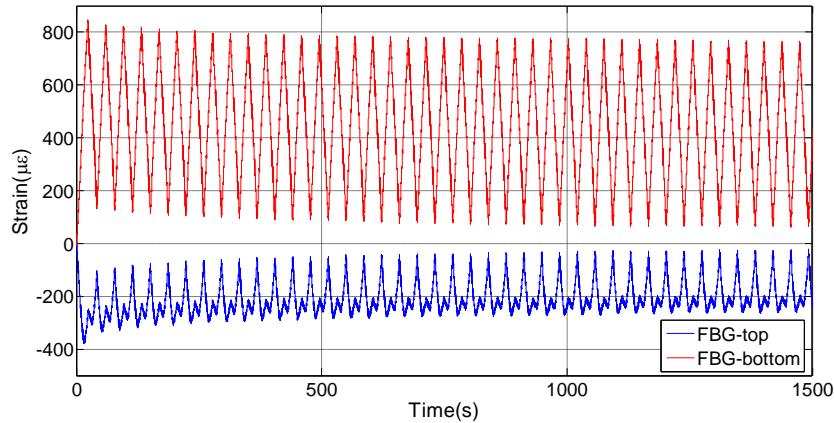
Figure 4.19: Strain responses of FBG sensors of SWC4 during the cyclic loading

Interestingly, the FBG sensor located in the compressive side of the sandwich specimen experiences two minimum strain values in each cycle, which might be attributed to the uneven strain fields generated in the proximity of the sensor as the loading applied from the upper support of the testing apparatus onto the glass tab placed underneath. Stress transfer through such geometry can result in dynamically varying strain gradients forming two distinct extremum points along the loading path of each cycle. Consequently, the damage parameter calculated based on this FBG sensor in the compressive facing shows abrupt changes after the first cycle leading to unreliable results. Moreover, as observed in the previous specimens, maximum and minimum strains of each cycle tend to decrease in the course of the experiment. Furthermore, recall that in SWC1, SWC2 and SWC3, the FBG sensors with the length of 10 mm and 1 mm, respectively are placed just underneath the upper loading support. Unlike SWC1 and SWC2, the reflected spectrum of the FBG sensor for SCW4 does not experience peak splitting under the cyclic loading, which is due to the shorter length of FBG sensor [28-29].

On the other hand, the damage parameter accumulation for the FBG in the tensile facing shows a similar trend observed in the previous test specimens as seen in Figure 4.20. The damage accumulation grows with declining rate as the cycling loading continues. Unlike SWC3 and similar to SWC2, the damage accumulation for SWC4 does not approach to a steady state even after 100 cycles, which can be associated with the application of cyclic loads with maximum standard travel close to the yield point. Furthermore, since the facing is made of fewer number of UD glass fiber layers compared to SWC3, higher vulnerability to damage can be expected causing persistent damage accumulation even after the 100 cycle. This FBG sensor also does not experience any significant change in the spectrum.
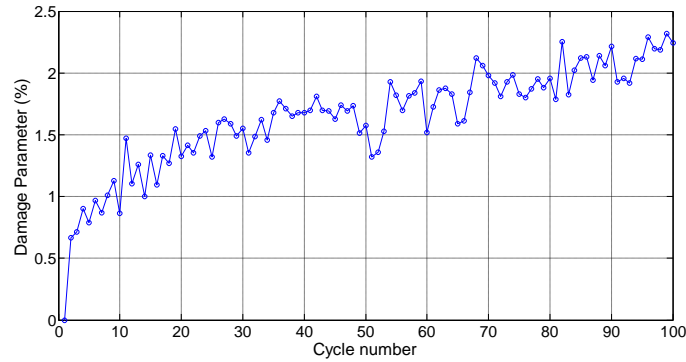
Figure 4.20: Damage parameter evolution for the below FBG embedded in SWC4 during cyclic loading.

In Figure 4.21 and 4.25, static test results of SWC5, SWC6 and SWC7 specimens without FBG sensors are provided. Being different from the initial 4 specimens, SWC5, SWC6 and SWC7 are manufactured using a core material with a higher density (i.e. 200 g/m^3) which can sustain through the thickness compressive loads thereby leading to improved resistance to core crushing. Accordingly, these sandwich specimens can withstand much higher standard deflections/deformations than the initial four sandwich samples without any considerable yielding. Higher resistance of the core enables the exploitation of the facing performance fully, hence making compressive facing rupture the dominant failure mode for the material system in question. The maximum standard travel applied onto the specimens during cyclic loading is 5 mm which is very low compared to the failure point of the material system. Figures 4.22, 4.27 and 4.28 give the variation of strain as a function of cycle number from which one may see that the minimum and maximum values of the strain for each cycle remain roughly the same in the course of loading, implying that the damage inflicted on the specimens is relatively small. Even though this maximum standard travel is larger than or same as those for previous test specimens, it does not damage the integrity of the samples significantly as shown in Figures 4.23 and 4.27 since the ratio of applied standard travel to the yield point is rather low in comparison to previous tests. It should be stated that the FBG spectrums for all of the specimens with high density core materials show insignificant shape variations their associated cyclic loading process.
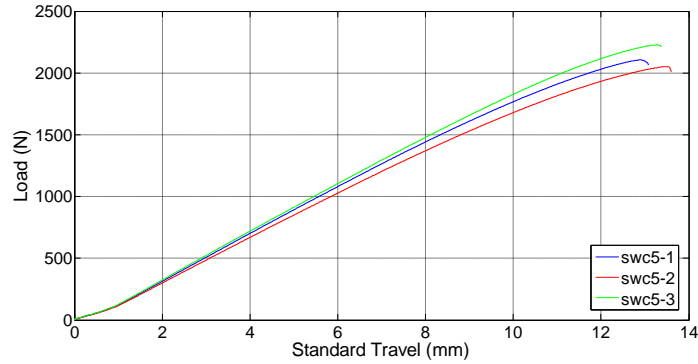
Figure 4.21: Static test results for SWC5 specimens without FBG.
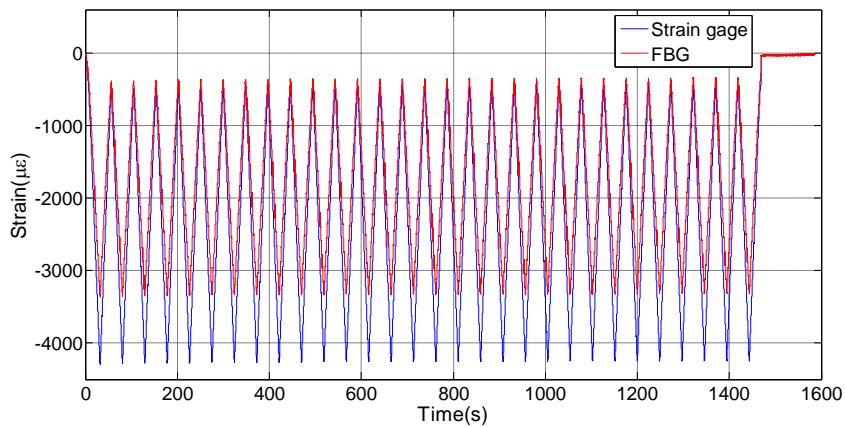
Figure 4.22: The variation of strain acquired by the strain gage and the FBG sensor during the cyclic loading for SWC5.
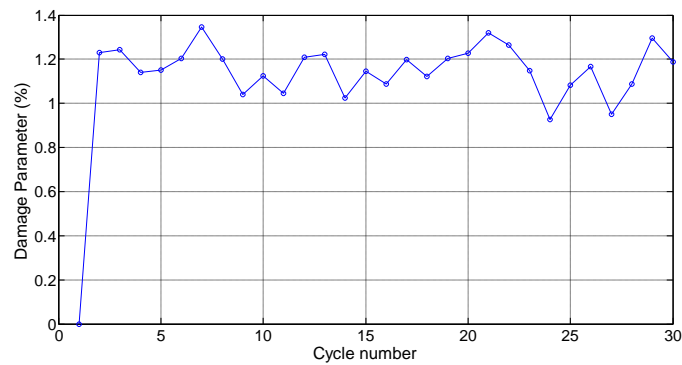
Figure 4.23: The evolution of the damage parameter evolution for SWC5.

All of the remaining specimens are exposed to static loading until failure. Figure 4.24 illustrates the variation of strain with time, acquired by the FBG sensor and strain gage for SWC5. The failure mode for the SWC5 specimen is the compressive failure of the facing as shown in Figure 4.25. It is demonstrated that sudden rupture of the facing due to compression results in a sharp drop in the wavelength (correspondingly strain) as it is illustrated in Figure 4.24. Strain measure from the FBG sensor experiences around 7000 $\mu\varepsilon$ strain drop reaching approximately to -1000 $\mu\varepsilon$ after the failure. No significant residual strain is measured by the

FBG sensor after the failure and spectrum response of the FBG sensor does not show any prominent shape distortion.
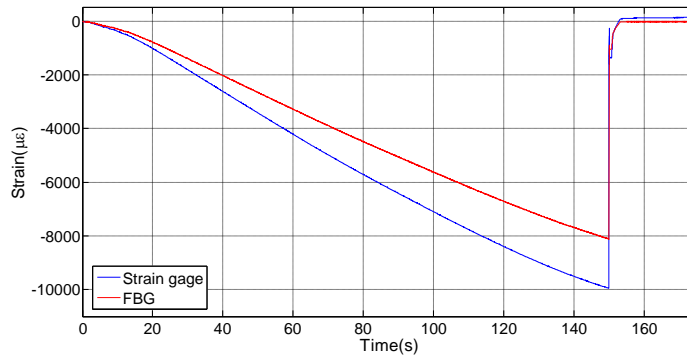
Figure 4.24: Strain evolution of strain gage and FBG sensor for SWC5.
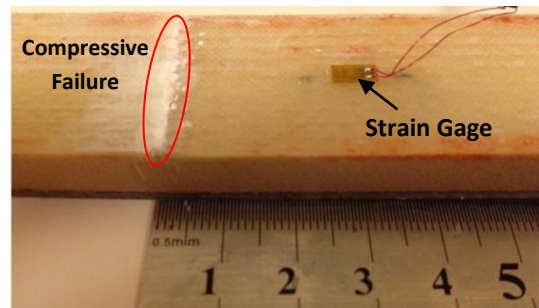
Figure 4.25: Specimen after compressive facing failure, FBG sensor is around 2 cm away from the failure point beneath the strain gage.

The SWC6 and SWC7 specimens are investigated for monitoring the response of the FBG sensor under the core shear failure damage mode. During the preliminary experiments with specimens without embedded FBG sensor, it is observed that lowering the span length in three-point flexural test does not trigger the core shear failure mode but rather results in indentation of the facing beneath the loading point. To trigger the core shear failure, a defect along the width of the specimen is artificially introduced in the core just above the bottom facing as shown in Figure 4.32 and 4.34. Corresponding static test results are provided in Figure 4.26 for bare specimens. Figure 4.27 and 4.28 illustrates the strain variations of the associated specimens for the cyclic loads. Finally, damage parameter evolutions are provided in Figure 4.29 which demonstrates minor variations for both of the specimens.
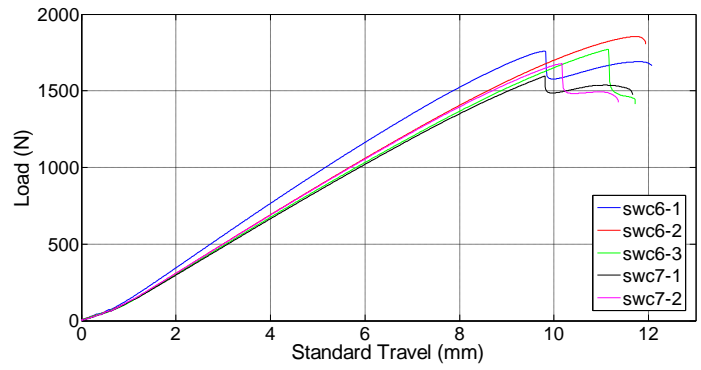
Figure 4.26: Static test results for SWC6 & SWC7 specimens without FBG.
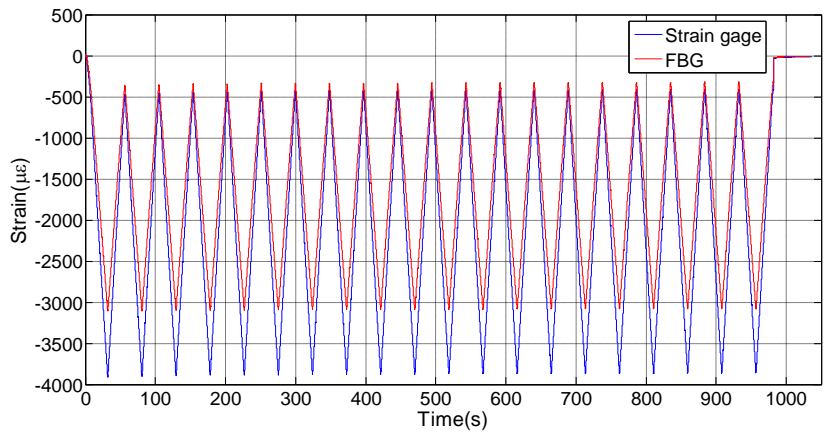
Figure 4.27: The variation of strain acquired by the strain gage and the FBG sensor during the cyclic loading for SWC6.
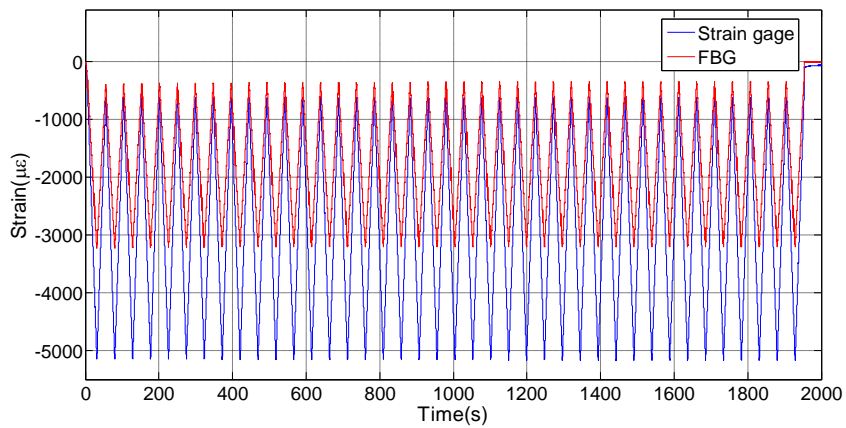

Figure 4.28: The variation of strain acquired by the strain gage and the FBG sensor during the cyclic loading for SWC7.
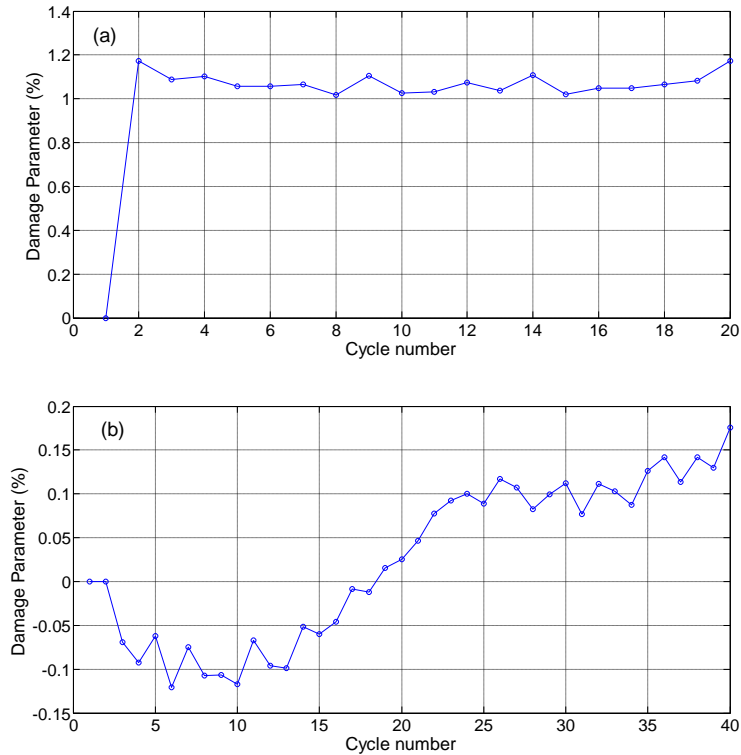
Figure 4.29: The evolution of the damage parameter evolution for SWC6 (a) and SWC7 (b).

After the cyclic loads, specimens SWC6 and SWC7 are exposed static loading until structural failure is achieved. For SWC6, artificial cutting is introduced 45 mm away from the loading support to cause the desired failure mode as illustrated in Figure 4.32. During the loading of SWC6, at strain level corresponding to -5000 $\mu\varepsilon$, the core shear failure occurs and the rapid propagation of the crack within the core causes imminent drop in the strain. As failure induces delamination between the compressive facing and the core, strain transfer between the two weakens resulting in a strain reduction. After the formation of core shear failure, structure continues to carry loads for 15s as it is partially intact. After this duration, severe bending of the facing along the delaminated region occurred resulting in substantial delamination between the facing and core over longer ranges within the gagelength. Moreover, after the removal of the load, spectrum splitting was spotted as can be seen in Figure 4.31. Such a response from the sensor can be attributed to the formation of uneven strain fields caused by the delamination beneath the facing. When the delamination terminates within the sensor gage length, strain fields become different between the intact and delaminated regions below the sensing region of the sensor leading to the observed peak splitting phenomena as demonstrated in the literature [20]. Furthermore, negligible amount of residual strain is measured from the FBG sensor after the failure.
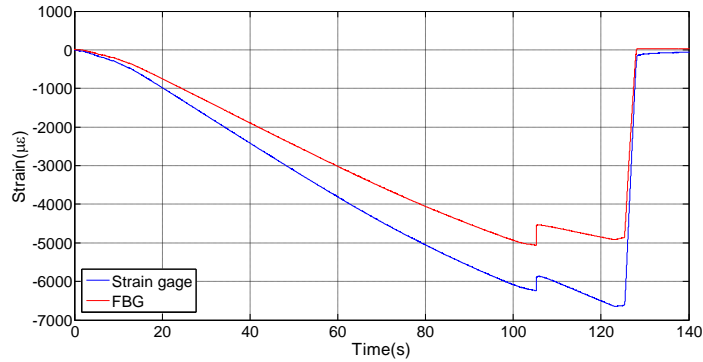
Figure 4.30: Strain evolution of strain gage and FBG sensor for SWC6
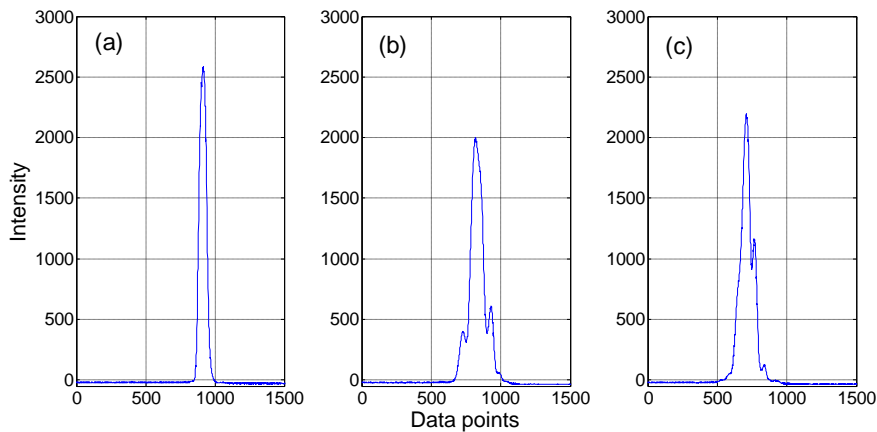
Figure 4.31: FBG spectrum response evolution for static loading until failure for SWC6, a) before the loading, b) during loading (around 127s after the start of the loading), c) after the loading.
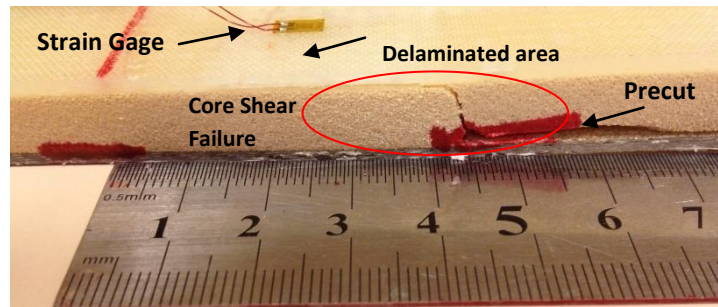
Figure 4.32: Specimen SWC6 after core shear failure, delamination stops along the gage length of the sensor located beneath the strain gage.

Strain variation of FBG and strain gage for SWC7 is given in Figure 4.33. For this specimen, artificial cutting is applied 20 mm away from the loading support as can be seen in Figure 4.34. Around 125 s, core-shear failure occurs. This time, severe bending of the core around the delaminated region occurs right after the core-shear failure unlike SWC6. Such an effect causes sudden reduction in strain around 2000 $\mu\varepsilon$ and strain measured from the sensor reaches -3300 $\mu\varepsilon$ before the removal of the load. Again, such a strain variation is attributed to the delamination associated with the failure formation. As artificial crack is induced closer to

the support location, delamination misses the sensor location and FBG in SWC7 does not experience two separate regions with different associated strain fields along its gagelength. As a result, peak splitting is not observed in the reflected spectrum of the specimen after the failure and removal of the load.
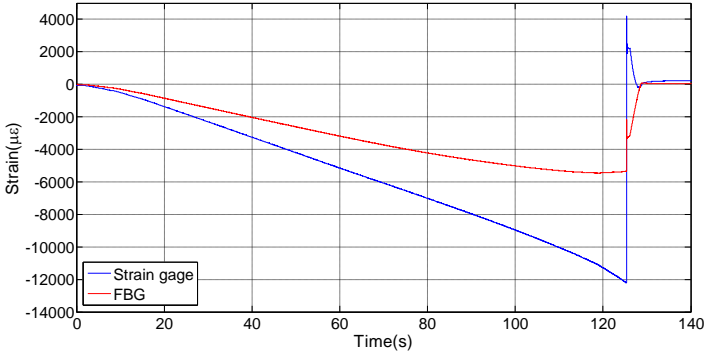
Figure 4.33: Strain evolution of strain gage and FBG sensor for SWC7
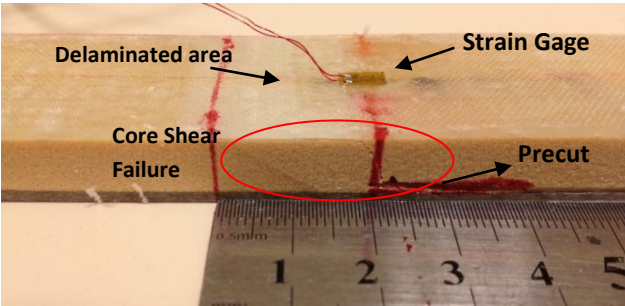
Figure 4.34: Specimen SWC 7 after core shear failure, delamination misses the gage length of the sensor located beneath the strain gage.

The comparison of strains measured by the FBG sensor during the loading (induced by previously mentioned 2mm standard travel) of intact and deformed specimens is provided in Table 4.2. It is noted that there is a considerable difference in the sensor responses especially for the first three specimens where the dominant failure mode is facing indentation. Such deviations from the original response might be attributed to the severity of the damage induced during the cycling process. FBG sensors within compressive facing of SWC1 and SWC4 experiences higher degree of damage formation as they are beneath the loading point where the indentation occurs leading to a considerable difference between the intact and deformed states. Table 4.2 also contains the residual strains in the specimens acquired by the FBG sensors after the cyclic loading of each specimen. The degree of damage formation can be related to the amount of residual strain in the specimen. Sensors experiencing indentation in their vicinity show noticeable amount of residual strains especially in the case of SWC1 for

61

which the damage accumulation is severe. For SWC5, SWC6 and SWC7, residual strains are not noteworthy as damage level is insignificant after the cyclic loading.

Table 4.2: Calculated strains in µε from FBG for the first and second 2mm standard travel application (St1, St2)

Specimen code	St1 strain(µε)	St2 strain(µε)	Strain change (%)	Residual strain(µε)
SWC1	-1188	-714	39.9	344
SWC2	-736	-700	4.9	-17
SWC3	-639	-540	15.5	65
SWC4(compressive)	-625	-351	43.8	88
SWC4(tension)	730	633	13.3	-47
SWC5	-1044	-1150	-10.2	-20
SWC6	-1091	-1116	-2.3	-8
SWC7	-1339	-1378	-2.9	1

The following remarks can be made on the performance of embedded FBG sensors for monitoring failure modes of foam cored sandwich structures under flexural loads so that FBG sensor based failure detection strategy can be developed.

▪ The indentation failure along the FBG sensor causes permanent distortion of the spectrum due to the compressive transverse strain states associated with the failure mode. However, as the FBG located further away from the failure point, the spectrum splitting is not observed after the failure.

▪ The cyclic loading can cause damage parameter accumulation which can grow with a decreasing rate. As the ratio of the maximum standard travel to the yield strength of the specimen increases, the damage accumulation tends to become higher and faster.

▪ Upon exposure to the same deflection, sensors can show distinct responses between deformed and un-deformed states suggesting damage formation in the vicinity of the FBG sensor. The observation of significant difference in the measured strains between the two cases can be ascribed to the facing indentations.

▪ The significant residual strain formation might be considered as the characteristic behavior for facing indentation failure as observed for the first four samples.

▪ Peak splitting is detected for FBG sensors that have indentation or core-shear failure along their gage length. Delamination location and severity of the indenting

determines the occurrence of peak splitting for core shear failure and facing indentation cases, respectively.

- Sudden strain drop is detected for the specimens experiencing compressive facing failure and core shear failure associated with the imminent deformation and rapid crack propagation. Quantity of the reduction is much higher for the compressive facing failure case.

- Among the specimens that undergo facing indentation, considerable rapid strain reduction was observed only for SWC1 at the first cycle of its cyclic loading. This effect can be attributed to the weaker structure of the facing compared to the other specimens as the structure is more prone to load concentrations causing low density core to crush prematurely. Nevertheless, compared to the other failure modes, strain reduction and its rate is much limited.

Accordingly, exploiting the sensor behavior in a variety of conditions, possible failure detection strategies can be achieved. If the sensor measures significant amount of residual strains compared to the initial unloaded state, it is highly probable that facing indentation occurs in the sensor location. The amount of residual strain can give qualitative information regarding the distance of the damage to the optical sensor. When reflected spectrum of the sensor splits into two peaks in the unloaded state, there is either core shear failure or facing indentation which can be decided based on the quantity of residual strain as core shear does not cause residual strains formation as much as indentation does. Additionally, higher distortions in the spectrum can be attributed to the indentation as such behavior is less likely to be seen after the core shear failure (delamination causes two distinct peaks). Moreover, if signal loss is detected, this may be the indication of either rupture or significant bending in the vicinity of the sensor alerting for the loss of structural integrity and may necessitate inspection in the related part. Checking for the strain relaxation behavior of the FBG sensors can also give valuable information regarding the nature of the failure as the compressive failure should cause higher imminent decrease in the strain compared to the core-shear failure and facing indentation cases during which strain decreases imminently in a lesser amount since the structure is partially intact after the failure. Strain drops for facing indentation and related core crushing cases is generally not expected and if it occurs its quantity and rate will be insignificant allowing easy differentiation from other failure modes.

4.4. Conclusion

In this study, structural monitoring and damage characterization of foam core sandwich composites are performed via FBG sensors embedded within sandwich facings. As the specimens subjected to static and cyclic loading conditions, changes in the spectrum and wavelength data is used to evaluate the damage and deformation in the material. Three different failure modes i.e. facing indentation, compressive facing and core shear failure were investigated and their effect on FBG sensors is analyzed. With the utilization of different sensor lengths and sensor information i.e. wavelength shift and reflected spectrum, damage detection and characterization can be achieved in sandwich composites. Overall, this work aims to enhance the understanding of how embedded FBG sensors behave under different damage modes and develop possible damage detection strategies to implement reliable structural health monitoring for sandwich structures.

CHAPTER 5

Conclusion

Fiber reinforced composites and their utilization in fabrication of sandwich structures offer many advantages to design components with outstanding properties for a variety of sectors offering considerable weight reductions, design flexibilities and fuel savings depending on the application. However, such benefits come at a price as these materials contain highly heterogeneous structure making prediction of their response to different loading and environmental conditions rather intricate. In order for better understanding of the material behavior and their internal damage state, structural health monitoring concept is proposed which is highly desirable for the evaluation of structural integrity of such components. Successful implementation of a structural health monitoring system enables real time examination of structures allowing significant cost reductions for their maintenance and more effective designs to lower safety factors and prevent overbuilt of the components by providing greater insight for the material behavior. In this context, Fiber Bragg Grating sensors have considerable potential for condition monitoring of the components to detect damage and monitor strains. One of the most crucial features of these sensors is their embedment capability within composite structures allowing evaluation of internal strain state of the material. In this research, this property of the sensors is utilized to assess the strain evolutions within the fiber reinforced and sandwich composites under different loading conditions. Moreover, this work also focuses on the examination of the sensor responses to different damage states and loads to evaluate feasibility of their performance.

Within this scope, for the first part of the thesis, signal acquisition of the FBG sensor embedded in a fiber reinforced composite that undergoes fatigue loading is studied. As fatigue loading continues, intermittent signal loss can occur threatening the reliability of the sensors for continual condition monitoring. Important factors that can affect the occurrence of the signal loss are proposed and discussed. Non-uniform strain fields formed in the course of the

fatigue loading along the vicinity of a FBG sensor can cause sensor to experience peak splitting in its reflected spectrum. In order to circumvent this problem, several practical issues regarding the sensor integration into the structures are needed to be considered to obtain signals continuously. These factors are sensor orientation with respect to the reinforcing fibers, tow width, sensor length and crack density. It is demonstrated that FBG sensors with 1 mm gagelength oriented parallel to the reinforcing fibers at the middle section of the laminate does not experience intermittent signal losses unlike the 10 mm FBG sensors that are located perpendicular to the reinforcing fibers. As the tows introduce non-uniform strain fields together with the resin rich regions, long FBG sensors in contact with such regions are more prone to peak splitting. Moreover, cracks occurred along the sensor can also form uneven strain fields in the vicinity of the sensor adding further risk to experience signal losses and as long FBG sensors have greater potential to interact with more cracks, they are more vulnerable to the peak splitting.

In the second part, fiber reinforced composites containing three embedded FBG sensors are exposed to constant, high strain fatigue loadings. Fatigue loads and desired maximum strains are imposed using both LVDT and extensometers. Sensor responses reveal that maximum strain measured in each cycle from the sensors can significantly differ from each other and they can decrease as fatigue loading continues. Strain reduction measured from the sensors tends to capture the fatigue phases of the composite in that particular local region. In general, there is a rapid reduction in the maximum strain followed by more gradual decrease and finally abrupt change of the maximum strain is observed corresponding to the third phase of the composite fatigue. Temperature distributions are also investigated revealing that they can also capture fatigue phases of the composite together with the strain energy and corresponding phase durations generally coincide with each other. Decline in maximum strain can be attributed to the decrease in the effective strain transfer between the reinforcing fibers and the FBG sensor due to the deformations and different damage modes formed in the vicinity of the FBG sensors. Important practical issues are discussed for implementation of constant strain fatigue tests such as sensor gagelengths.

For the final part, failure modes of foam cored sandwich structures i.e. facing indentation, compressive facing and core shear failure are monitored using embedded FBG sensors. Utilizing the sensor response of both wavelength change and shape of the reflected spectrum, possible damage detection strategy is proposed. Damage modes are characterized based on the detection of residual strains, peak distortions and sudden strain variations obtained from the embedded sensors. FBG sensors within sandwich beams experiencing

facing indentation detected residual strain formation and showed peak distortions depending on the sensor location. FBG sensors showed sudden strain decrease in the case of compressive and core shear failure of the sandwich beams with higher decrease in the former case.

This research offers several insights regarding the strain measurement of FBG sensors. Strain transfer from the host material to FBG sensor can significantly change over the course of loading. Moreover, induced strain transfer for the FBG sensors may result in strains that can be different in magnitude than the strain of the host material. Even though there are substantial amount of work, sensor calibration is still an issue that needs to be addressed in order for broader and more reliable application of this technology to perform SHM of composite structures. Nevertheless, FBG sensors are capable of providing valuable information regarding the internal state of the material and compared to the other sensor technologies that allows internal embedment capability, FBG sensors offers one of the most promising technology for such a task. Understanding the internal state of the material is highly valuable as internal material state can be significantly different from the global behavior of the material depending on various factors. As it is repeatedly observed in this thesis, there can be considerable disperancy between the local and global material responses which is very crucial phenomenon to consider in design especially for structures containing high inherent heterogeneities. Moreover, different information such as change in the reflected wavelength and spectrum of the light can be utilized to assess the damage within the composite structure. Performance of the FBG sensors is evaluated and their potential capability for monitoring internal state of the material is demonstrated. As a future work, different reinforcement fibers can be used to understand the effect of different materials on the response of the FBG sensors both in terms of spectrum shape and wavelength of the reflected light. Different loading scenarios can also be investigated for the fatigue performance of the FBG sensors by changing the frequency and amplitude of the cyclic loads.

References

[1] D.D.L. Chung, Composite Materials: Science and Applications, Springer-Verlag London Limited, 2003.

[2] B. Harris, Fatigue in composites, Woodhead Publishing Limited, Cambridge, England, 2003.

[3] V. Natarajan, H.V.S. Gangarao, and V. Shekar, Fatigue Response of Fabric-reinforced Polymeric Composites, Journal of Composite Materials, Volume 39, Issue 17, September 2005, Pages 1541-1559, doi:10.1177/0021998305051084

[4] A. Othonos, K. Kalli, G.E. Kohnke, Fiber Bragg Gratings: Fundamentals and Applications in Telecommunications and Sensing, Artech House Inc., Boston, Massachusetts, (1999).

[5] A. Cusano, A. Cutolo and J. Albert, Fiber Bragg grating sensors: recent advancements, industrial applications and market exploitation, ISBN: 978-1-60805-343-8, doi: 10.2174/97816080508401110101.

[6] G. Luyckx, E. Voet, N. Lammens and J. Degrieck, Strain Measurements of Composite Laminates with Embedded Fibre Bragg Gratings: Criticism and Opportunities for Research, Sensors 2011, 11(1), 384-408; doi:10.3390/s110100384.

[7] G. Berruti, M. Consales, M. Giordano, L. Sansone, P. Petagna, S. Buontempo, G. Breglio, A. Cusano, Radiation hard humidity sensors for high energy physics applications using polyimide-coated fiber Bragg gratings sensors, Sensors and Actuators B: Chemical, Volume 177, February 2013, Pages 94-102, ISSN 0925-4005, doi:10.1016/j.snb.2012.10.047.

[8] G. Rajan, Y.M. Noor, B. Liu, E. Ambikairaja, D.J. Webb, G.D. Peng, A fast response intrinsic humidity sensor based on an etched singlemode polymer fiber Bragg grating, Sensors and Actuators A: Physical, Volume 203, 1 December 2013, Pages 107-111, ISSN 0924-4247, doi:10.1016/j.sna.2013.08.036.

[9] X. Fan, I.M. White, S.I. Shopova, H. Zhu, J.D. Suter, Y. Sun, Sensitive optical biosensors for unlabeled targets: A review, Analytica Chimica Acta, Volume 620, Issues 1–2, 14 July 2008, Pages 8-26, ISSN 0003-2670, doi:10.1016/j.aca.2008.05.022.

[10] M. Majumder, T. K. Gangopadhyay, A.K. Chakraborty, K. Dasgupta, D.K. Bhattacharya, Fibre Bragg gratings in structural health monitoring—Present status and applications, Sensors and Actuators A: Physical, Volume 147, Issue 1, 15 September 2008, Pages 150-164, ISSN 0924-4247, doi:10.1016/j.sna.2008.04.008.

[11] C.Y. Lin, L.A. Wang, G.W. Chern, "Corrugated long-period fiber gratings as strain, torsion, and bending sensors," Lightwave Technology, Journal of , vol.19, no.8, pp.1159,1168, Aug 2001, doi: 10.1109/50.939797.

[12] H.F. Pei, J. Teng, J.H. Yin, R. Chen, A review of previous studies on the applications of optical fiber sensors in geotechnical health monitoring, Measurement, Volume 58, December 2014, Pages 207-214, ISSN 0263-2241, doi:10.1016/j.measurement.2014.08.013.

[13] R. Maaskant, T. Alavie, R.M. Measures, G. Tadros, S.H. Rizkalla, A. Guha-Thakurta, Fiber-optic Bragg grating sensors for bridge monitoring, Cement and Concrete Composites, Volume 19, Issue 1, 1997, Pages 21-33, ISSN 0958-9465, doi:10.1016/S0958-9465(96)00040-6.

[14] T.H.T. Chan, L. Yu, H.Y. Tam, Y.Q. Ni, S.Y. Liu, W.H. Chung, L.K. Cheng, Fiber Bragg grating sensors for structural health monitoring of Tsing Ma bridge: Background and experimental observation, Engineering Structures, Volume 28, Issue 5, April 2006, Pages 648-659, ISSN 0141-0296, doi:10.1016/j.engstruct.2005.09.018.

[15] R.C. Tennyson, A.A. Mufti, S. Rizkalla, G. Tadros and B. Benmokrane, Structural health monitoring of innovative bridges in Canada with fiber optic sensors, Smart Materials and Structures, Volume 10, Issue 3, 2001, Page 560, doi:10.1088/0964-1726/10/3/320.

[16] Y. Okabe, S. Yashiro, T. Kosaka, N. Takeda, Detection of transverse cracks in CFRP composites using embedded fiber Bragg grating sensors, Smart Materials and Structures, Volume 9, Issue 6, 2000, Page 832, doi:10.1088/0964-1726/9/6/313.

[17] Y. Okabe, T. Mizutani, S. Yashiro, N. Takeda, Detection of microscopic damages in composite laminates with embedded small-diameter fiber Bragg grating sensors, Composite Science and Technology, Volume 62, 2002, 951-958.

[18] Y. Okabe, R. Tsuji, N. Takeda, Application of chirped fiber Bragg grating sensors for identification of crack locations in composites, Composites Part A: Applied Science and Manufacturing, Volume 35, Issue 1, January 2004, Pages 59-65, ISSN 1359-835X, doi:10.1016/j.compositesa.2003.09.004.

[19] N. Takeda, Y. Okabe, J. Kuwahara, S. Kojima, T. Ogisu, Development of smart composite structures with small-diameter fiber Bragg grating sensors for damage detection: Quantitative evaluation of delamination length in CFRP laminates using Lamb wave sensing, Composites Science and Technology, Volume 65, Issues 15–16, December 2005, Pages 2575-2587, ISSN 0266-3538, doi:10.1016/j.compscitech.2005.07.014.

[20] S. Takeda, Y. Okabe, N. Takeda, Delamination detection in CFRP laminates with embedded small-diameter fiber Bragg grating sensors, Composites Part A: Applied Science and Manufacturing, Volume 33, Issue 7, 1 July 2002, Pages 971-980, ISSN 1359-835X, doi:10.1016/S1359-835X(02)00036-2.

[21] N. Takeda, Characterization of microscopic damage in composite laminates and real-time monitoring by embedded optical fiber sensors, International Journal of Fatigue, Volume 24, Issues 2–4, February–April 2002, Pages 281-289, ISSN 0142-1123, http://dx.doi.org/10.1016/S0142-1123(01)00083-4.

[22] S. Yashiro, N. Takeda, T. Okabe, H. Sekine, A new approach to predicting multiple damage states in composite laminates with embedded FBG sensors, Composites Science and Technology, Volume 65, Issues 3–4, March 2005, Pages 659-667, ISSN 0266-3538, doi:10.1016/j.compscitech.2004.09.022.

[23] N. Takeda, S. Yashiro, T. Okabe, Estimation of the damage patterns in notched laminates with embedded FBG sensors, Composites Science and Technology, Volume 66, Issue 5, May 2006, Pages 684-693, ISSN 0266-3538, doi:10.1016/j.compscitech.2005.07.039.

[24] C. Doyle, A. Martin, T. Liu, M. Wu, In-situ process and condition monitoring of advanced fibre-reinforced composite materials using optical fibre sensors, Smart Materials and Structures, Volume 7, Issue 2, 1998, Page 145, doi:10.1088/0964-1726/7/2/002.

[25] I. De Baere, G. Luyckx, E. Voet, W. Van Paepegem, J. Degrieck, On the feasibility of optical fibre sensors for strain monitoring in thermoplastic composites under fatigue loading

conditions, Optics and Lasers in Engineering, Volume 47, Issues 3–4, March–April 2009, Pages 403-411, ISSN 0143-8166, doi:10.1016/j.optlaseng.2008.01.001.

[26] D.C. Betz, G. Thursby, B. Culshaw, W.J. Staszewski. Acousto-ultrasonic sensing using fiber Bragg gratings, Smart Materials and Structures, Volume 12, Issue 1, 2003, Page 122, doi:10.1088/0964-1726/9/6/313.

[27] H. Tsuda, Ultrasound and damage detection in CFRP using fiber Bragg grating sensors, Composites Science and Technology, Volume 66, Issue 5, May 2006, Pages 676-683, ISSN 0266-3538, doi:10.1016/j.compscitech.2005.07.043.

[28] K. Peters, M. Studer, J. Botsis, A. Iocco, H. Limberger, R. Salathe. Embedded optical fiber Bragg grating sensor in a nonuniform strain field: Measurements and simulations, Experimental Mechanics, Volume 41, Issue 1, March 2001, Page 19-28.

[29] P. Kara, P. Pattis, J. Botsis, P. Giaccari, Experimental verification of response of embedded optical fiber Bragg grating sensors in non-homogeneous strain fields, Optics and Lasers in Engineering, Volume 33, Issue 2, 2000, 107-119, doi: 10.1016/S0143-8166(00)00033-6.

[30] Y. Okabe, S. Yashiro, R. Tsuji, T. Mizutani, N. Takeda, Effect of thermal residual stress on the reflection spectrum from FBG sensors embedded in CFRP composites, Proc. SPIE 4704, Nondestructive Evaluation and Health Monitoring of Aerospace Materials and Civil Infrastructures, 59 (June 18, 2002), doi:10.1117/12.470709.

[31] C.J. Keulen, E. Akay, F.F. Melemez, E.S. Kocaman, A. Deniz, C. Yilmaz, T. Boz, M. Yildiz, H.S. Turkmen, A. Suleman, Prediction of fatigue response of composite structures by monitoring the strain energy release rate with embedded fiber Bragg gratings, Journal of Intelligent Material Systems and Structures, December 9, 2014, doi: 10.1177/1045389X14560358.

[32] C. J. Keulen, M. Yildiz, A. Suleman, Multiplexed FBG and etched fiber sensors for process and health monitoring of 2-&3-D RTM components, Journal of Reinforced Plastics and Composites, Volume 30, No:12, June 2011, 1055-1064, doi:10.1177/0731684411411960

[33] M. Yildiz, N.G. Ozdemir, G. Bektas, C.J. Keulen, T. Boz, E.F. Sengun, C. Ozturk, Y.Z. Menceloglu, A. Suleman, An experimental study on the process monitoring of resin transfer molded composite structures using fiber optic sensors, Journal of Manufacturing Science and Engineering, Volume 134, Issue 4, 2012, 044502 (6 pages) doi:10.1115/1.4006770.

[34] V.M. Murukeshan, P.Y. Chan, L.S. Ong, L.K. Seah, Cure monitoring of smart composites using Fiber Bragg Grating based embedded sensors, Sensors and Actuators A: Physical, Volume 79, Issue 2, 1 February 2000, Pages 153-161, ISSN 0924-4247, doi:10.1016/S0924-4247(99)00266-6.

[35] Sandwich composites and core materials, How they work and why you should use them. DIAB.

[36] L.A. Carlsson, G.A. Kardomateas, Structural and Failure Mechanics of Sandwich Composites, 2011.

[37] M.S. Konsta-Gdoutos, E.E. Gdoutos. The Effect of Load and Geometry on the Failure Modes of Sandwich Beams, Applied Composite Materials, Volume 12, Issue 3-4, 2005, Pages 165-176.

[38] T.S. Lim, C.S. Lee, D.G. Lee. Failure Modes of Foam Core Sandwich Beams under Static and Impact Loads, Journal of Composite Materials, Volume 38, Issue 18, 2004, Pages 1639-1662, doi: 10.1177/0021998304044760.

[39] C.A. Steeves, N.A. Fleck, Collapse mechanisms of sandwich beams with composite faces and a foam core, loaded in three-point bending. Part I: analytical models and minimum weight design, International Journal of Mechanical Sciences, Volume 46, Issue 4, April 2004, Pages 561-583, ISSN 0020-7403, doi:10.1016/j.ijmecsci.2004.04.003.

[40] R.F. Gibson. A Mechanics of Materials/Fracture Mechanics Analysis of Core Shear Failure in Foam Core Composite Sandwich Beams, Journal of Sandwich Structures and Materials, Volume 13, Issue 1, 2011, Pages 83-95, doi: 10.1177/1099636209359843.

[41] A. Chemami, K. Bey, J. Gilgert, Z. Azari, Behaviour of composite sandwich foam-laminated glass/epoxy under solicitation static and fatigue, Composites Part B: Engineering, Volume 43, Issue 3, April 2012, Pages 1178-1184, ISSN 1359-8368, doi:10.1016/j.compositesb.2011.11.051.

[42] E. Farmand-Ashtiani, J. Cugnoni, J. Botsis, Monitoring and characterization of the interfacial fracture in sandwich composites with embedded multiplexed optical sensors, Composite Structures, Volume 96, February 2013, Pages 476-483, ISSN 0263-8223, doi:10.1016/j.compstruct.2012.08.059.

[43] D. Hackney, K. Peters. Damage Identification After Impact in Sandwich Composites Through Embedded Fiber Bragg Sensors, Journal of Intelligent Materials Systems and Structures, Volume 22, Issue 12, 2011, Pages 1305-1316, doi: 10.1177/1045389X11414220.

[44] K.S.C. Kuang, L. Zhang, W.J. Cantwell, I. Bennion, Process monitoring of aluminum-foam sandwich structures based on thermoplastic fibre–metal laminates using fibre Bragg gratings, Composites Science and Technology, Volume 65, Issues 3–4, March 2005, Pages 669-676, ISSN 0266-3538, doi:10.1016/j.compscitech.2004.09.005.

[45] K.S.C. Kuang, W.J. Cantwell, L. Zhang, I. Bennion, M. Maalej, S.T. Quek, Damage monitoring in aluminum-foam sandwich structures based on thermoplastic fibre-metal laminates using fibre Bragg gratings, Composites Science and Technology, Volume 65, Issues 11–12, September 2005, Pages 1800-1807, ISSN 0266-3538, doi:10.1016/j.compscitech.2005.03.009.

[46] P.E. Bourban, W.J. Cantwell, H.H. Kausch, S.J. Youd. Damage initiation and development in chopped strand mat composites. Proc ICCM 9, 1993, 5:79–86.

[47] ASTM (D3479), Standard Test Method for Tension-Tension Fatigue of Polymer Matrix Composite Materials, 2010.

[48] J. Lindemann, W. Becker, The tendency for free-edge delamination in laminates and its minimization, Composites Science and Technology, Volume 62, Issue 2, February 2002, Pages 233-242, ISSN 0266-3538, doi:10.1016/S0266-3538(01)00214-7.

[49] S. Giancane, F.W. Panella, R. Nobile, V. Dattoma, Fatigue damage evolution of fiber reinforced composites with digital image correlation analysis, Procedia Engineering, Volume 2, Issue 1, April 2010, Pages 1307-1315, ISSN 1877-7058, doi:10.1016/j.proeng.2010.03.142.

[50] M. Naderi, M.M. Khonsari, On the role of damage energy in the fatigue degradation characterization of a composite laminate, Composites Part B: Engineering, Volume 45, Issue 1, February 2013, Pages 528-537, ISSN 1359-8368, doi:10.1016/j.compositesb.2012.07.028.

[51] ASTM (C393-00), Standard Test Method for Flexural Properties of Sandwich Constructions, 2000.

[52] P.E. Bourban, W.J. Cantwell, H.H. Kausch, S.J. Youd. Damage initiation and development in chopped strand mat composites. Proc ICCM 1993, 5:79–86.